



RESEARCH ARTICLE | DECEMBER 04 2023

# Motion of a two-dimensional neutrally buoyant circular particle in two-sided lid-driven cavity flow with thermal convection

Yunxin Zhang (张鑫鑫); Chenggong Li (李承功); Mao Ye (叶茂)  

 Check for updates

*Physics of Fluids* 35, 123305 (2023)

<https://doi.org/10.1063/5.0169369>

  
View  
Online

  
Export  
Citation

 CrossMark

## AIP Advances

Why Publish With Us?



**25 DAYS**  
average time  
to 1st decision



**740+ DOWNLOADS**  
average per article



**INCLUSIVE**  
scope

[Learn More](#)

 AIP  
Publishing

# Motion of a two-dimensional neutrally buoyant circular particle in two-sided lid-driven cavity flow with thermal convection

Cite as: Phys. Fluids **35**, 123305 (2023); doi: 10.1063/5.0169369

Submitted: 25 July 2023 · Accepted: 7 November 2023 ·

Published Online: 4 December 2023



View Online



Export Citation



CrossMark

Yunxin Zhang (张鑫),<sup>1,2</sup> Chenggong Li (李承功),<sup>1</sup> and Mao Ye (叶茂)<sup>1,a)</sup> 

## AFFILIATIONS

<sup>1</sup>National Engineering Research Center of Lower-Carbon Catalysis Technology, Dalian Institute of Chemical Physics, Chinese Academy of Sciences, Dalian 116023, China

<sup>2</sup>University of Chinese Academy of Sciences, Beijing 100049, China

<sup>a)</sup> Author to whom correspondence should be addressed: [maoye@dicp.ac.cn](mailto:maoye@dicp.ac.cn)

## ABSTRACT

Understanding the interaction between a cold particle and confined fluid flow is of practical importance in many industrial applications. In this work, the motion of a two-dimensional circular neutrally buoyant particle in thermal flows in the two-sided lid-driven cavity has been numerically investigated by the lattice Boltzmann model with immersed boundary method. We examined the effects of Grashof number ( $Gr$ ) and Reynolds number ( $Re$ ) of cavity on the motion of particle in the range of  $10^4 \leq Gr \leq 10^7$  and  $500 \leq Re \leq 3000$ . It is found that the motion of the cold particle in the cavity flow manifests four different modes, driven by the competition between buoyancy-driven natural convection and lid-driven forced convection. With the increase in  $Gr$  or the decrease in  $Re$ , the motion of the cold particle would evolve from modes I to IV. We further obtained the diagram of motion modes of the cold particle with regard to  $Gr$  and  $Re$ . And a power law correlation that relates the critical  $Gr$  to  $Re$  of the cavity is proposed and capable of well predicting the transition of particle motion modes.

Published under an exclusive license by AIP Publishing. <https://doi.org/10.1063/5.0169369>

## I. INTRODUCTION

The fluid–solid two-phase flow is of significant importance in the engineering and industrial practices, which is usually accompanied by the heat transport phenomena.<sup>1–3</sup> The research on the particle motion behavior in the two-phase flow coupling with heat transfer not only plays a fundamental role in understanding the underlying mechanics of momentum and heat transfer in the particulate two-phase flows, but also offers theoretical guidance in the practices of designing and optimizing industrial facilities. Furthermore, the confined flow, e.g., the lid-driven cavity flow, has been extensively investigated for its simple physical geometry but complex flow structures.<sup>4</sup> In the meantime, the particle motion in the confined fluid flow has also attracted abundant attention in various applications, including the rotary kilns,<sup>5</sup> the mixing tank,<sup>6</sup> and the polymerization reactors.<sup>7</sup> The single lid-driven cavity represents the simplest configuration and has been extensively studied.<sup>8–10</sup> Hwang *et al.*<sup>11</sup> investigated the free motion of neutrally buoyant particles in a single lid-driven cavity and found it could induce a chaotic advection flow. Tsornig *et al.*<sup>12,13</sup> experimentally studied the motion of near neutrally buoyant particles in the single lid-driven cavity using the stereoscopic imaging, in which they found that

the particles tend to move along the preferential orbits at the periphery of cavity at certain Reynolds and Stokes numbers. Shen *et al.*<sup>14</sup> quantitatively measured the velocity and trajectory of a neutrally buoyant spherical particle in the microcavity, which enabled the determination of the exerting forces acting on the particle during each phase of particle motion. Kosinski *et al.*<sup>15</sup> simulated the motions of many particles in a single lid-driven cavity in the absence of gravity through a Eulerian–Lagrangian approach, showing that the particles tend to migrate toward the walls and the migration can be enhanced at the higher Stokes number. Romanò and Kuhlmann<sup>16</sup> further showed that the motion of a single particle in the single lid-driven cavity follows a steady periodic orbit called limit cycle, which can be ascribed to the balance between the centrifugal and boundary repulsive forces and affected by the particle size and density. Later on, motivated by the interest in complex flow topology, the classical single lid-driven cavity problems were extended to those with two opposite moving walls,<sup>17</sup> i.e., the two-sided lid-driven cavity problems. Romanò *et al.*<sup>18</sup> conducted three-dimensional simulations on the motion of particles in a two-sided lid-driven cavity based on a one-way-coupling approach in which the gravity is ignored. They found that the initially randomly

distributed particles are attracted to the pair of point-symmetrical limit cycles, and these coherent structures could be affected by the particle density and diameter. Wu *et al.*<sup>19</sup> experimentally investigated the motion of single particle with various densities and diameters in a two-sided lid-driven cavity, in which they observed that the symmetry of limit cycles could be broken by the presence of gravity, and the trajectories of the particle are periodic or quasi-periodic. They also found that the buoyancy and inertia become important as the density mismatch between particle and fluid increase.<sup>20</sup> Hu<sup>21</sup> numerically studied the two-sided lid-driven cavity flow with an enclosing circular particle by the use of the fully resolved immersed boundary lattice Boltzmann method (IB-LBM). The results showed that the orbits of the limit cycles of the particle are affected by the cavity Reynolds number, in addition to the particle diameter.

Note that most of the previous studies on the motion of particles in the cavity were limited to the isothermal cases. In fact, it has been demonstrated that the thermal convection can affect the interaction between particles and fluid in the fluid-particle systems.<sup>22–24</sup> Much effort has been made for understanding the hydrodynamics forces and heat transfer phenomena in the thermal two-phase flow. For example, Feng and Michaelides<sup>25</sup> studied the non-isothermal particle sedimentation in channel by the immersed boundary method (IBM). The results showed that the heat advection increases the drag coefficient of hotter particles at relatively low Reynolds numbers, but reduces the drag coefficient of the colder particles at low and medium Reynolds numbers. Also, the particle motion can be altered in the presence of the buoyancy effect. Gan *et al.*<sup>26</sup> studied the sedimentation of a cold particle in a thermal channel and showed that several regimes can be identified for the settling behaviors of the particle in terms of Grashof number that scales the thermal buoyant force. Yang *et al.*<sup>27</sup> investigated the sedimentation of double particles in thermal condition by the lattice Boltzmann method with immersed boundary method and observed the enhanced drafting, kissing, and tumbling (DKT) phenomenon in the presence of the thermal convection effect. Moreover, the particle motions in the horizontal channels with the thermal convection have also been studied. Hu and Guo<sup>28</sup> studied the lateral migration of a single cold particle in the thermal Poiseuille flow. The symmetric particle equilibrium positions along the centerline in the isothermal state according to Segré and Silberberg<sup>29</sup> would migrate toward the bottom wall due to the thermal convection. In addition, the equilibrium positions are insensitive to the initial locations beyond a critical Grashof number. However, Liu and Wu<sup>30</sup> pointed out that the critical Grashof number, which is closely related to the equilibrium position transition, is a function of the channel Reynolds number and particle diameter. Furthermore, Liu and Wu<sup>31</sup> investigated the lateral migration of cold particle in the thermal Couette flow by the lattice Boltzmann method and found that the equilibrium positions can be characterized by the Richardson number and particle size. From the above studies, it can be found that the particle motion in fluid flow can be more complicated in the presence of heat transfer between particle and fluid.

In this work, we focus on the motion of a single particle in the two-sided lid-driven thermal flow. In spite of the simple geometry, the lid-driven cavity flow exhibits numerous fluid flow phenomena only found in the confined flows.<sup>5–7,32</sup> For instance, as previously unveiled,<sup>18–21</sup> a particle in the two-sided lid-driven cavity flow would demonstrate specific steady or quasi-periodic trajectories in the

isothermal state. This differs significantly from the flow patterns in the open configurations such as Couette flows and Poiseuille flows, which are generally attributed to the interplay between the forced and natural convection in thermal cavity flow. In this regard, the current study is expected to provide an insightful view on the evolution of particle motion in the confined thermal flows in which both the forced convection and natural convection play an important role. The fully resolved simulations based on a thermal lattice Boltzmann method coupled with the immersed boundary method are implemented for the particle motion in the two-sided lid-driven cavity flow. For simplicity, a neutrally buoyant particle is considered. The influences of cavity Grashof number and Reynolds number on the fluid-particle interaction and the particle motions are discussed in detail. The two-dimensional studies have been considered owing to the compromise between high computational cost and high resolution for the particle-resolved simulations. Despite that the three-dimensional simulations could capture more complex reality of fluid flow and particle motion, two-dimensional simulations are still able to reveal some very important information with relatively cheap computational cost suppose the common physics behind the two-dimensional and three-dimensional configurations can be correctly implemented. For example, the steady trajectory of a particle in a two-dimensional two-sided lid-driven cavity flow is a centrosymmetric limit cycle,<sup>21</sup> which, meantime, can similarly become a pair of limit cycles point-symmetrically located with respect to the cavity center in a three-dimensional configuration,<sup>17,18</sup> which could be ascribed to the particle-wall interaction.<sup>17</sup> The Segré-Silberberg effect,<sup>29</sup> known as the initially uniform and dilute suspended particles collecting into a thin, annular region in the three-dimensional Poiseuille flow, could be evolved into two equilibrium positions of particles located separately at two sides along the centerline in two-dimensional cases.<sup>30</sup> Hence, the simulations in three-dimensional two-sided cavity flow were also conducted in the present work to qualitatively reflect the difference between the motion of a spherical particle in two-dimensional and three-dimensional configurations.

The paper is organized as follows: the research objective and numerical method are first introduced in Secs. II and III, and the model is validated in Sec. IV. Then in Sec. V, the fluid-particle interaction and the particle motion with the varying Grashof number and Reynolds number are discussed, which is closed with some conclusions in Sec. VI.

## II. PROBLEM FORMULATION

Here, the motion of a two-dimensional neutrally buoyant particle in the two-sided lid-driven cavity flow with thermal convection is studied. As shown in Fig. 1, the square cavity considered has the length of  $L$  and is filled with the incompressible Newtonian fluid of density  $\rho_f$ . The fluid flow in the cavity is driven by the two boundary walls (i.e., top and bottom walls) moving oppositely with a uniform speed of  $U$  along  $x$ -direction. The top wall at  $y = L$  moves rightwards, and the bottom wall at  $y = 0$  moves leftwards. A constant temperature of  $T_h = 1$  is assumed for both the top and bottom walls. A circular particle with diameter  $d_p$  is placed in the cavity, which can move freely in the translational and rotational directions. The surface temperature of the particle is set to zero. Note that the left and right walls are assumed to be adiabatic ( $\partial T/\partial x = 0$ ), and the temperature of the fluid in the cavity is initially taken as  $T_h = 1$ . In this work, the particle is further

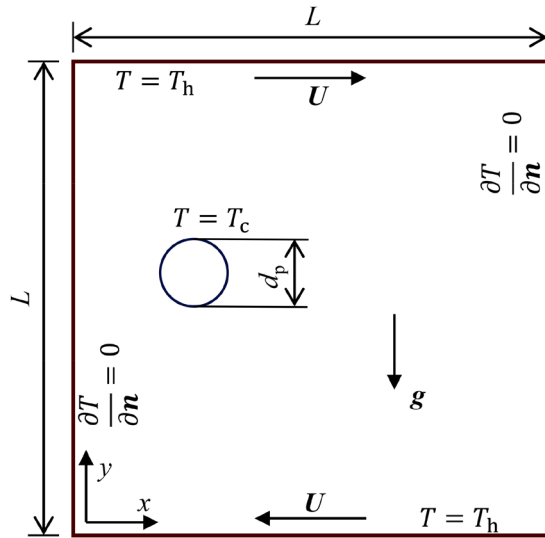


**FIG. 1.** The sketch of a neutrally buoyant particle in the two-sided lid-driven cavity flow with thermal convection.

considered to be neutrally buoyant, i.e., the density of the particle  $\rho_p$  is equal to that of the surrounding fluid  $\rho_f$  ( $\rho_p = \rho_f$ ).

The motion of a particle can be described by the Newtonian laws. The thermal flow in the cavity is described by the Navier–Stokes equations together with the energy equation,

$$\nabla \cdot \mathbf{u} = 0, \tag{1}$$

$$\frac{\partial \mathbf{u}}{\partial t} + \mathbf{u} \cdot \nabla \mathbf{u} = -\frac{1}{\rho_f} \nabla p + \nu \nabla^2 \mathbf{u} + \mathbf{F}, \tag{2}$$

$$\frac{\partial T}{\partial t} + \mathbf{u} \cdot \nabla T = \alpha \nabla^2 T + Q, \tag{3}$$

where  $\mathbf{u}$  is the macroscopic velocity,  $t$  is time,  $p$  is pressure,  $\nu$  is kinematic viscosity,  $\alpha$  is thermal diffusivity,  $T$  is temperature, and  $Q$  is the heat generation term. Note that  $\mathbf{F}$  is the body force term consisting of the buoyant force term  $\mathbf{F}_B$ . To obtain  $\mathbf{F}_B$ , the customary Boussinesq approximation frequently used in the research of the thermal fluid flows<sup>26,30,46</sup> has been employed, in which it is assumed that the temperature change only modifies the fluid density  $\rho_f$  in the body force term,<sup>26</sup> namely,

$$\rho_f = \rho_0 [1 - \beta(T - T_0)], \tag{4}$$

where  $\beta$  is the coefficient of thermal expansion,  $T_0$  is the average temperature of the fluid, and  $\rho_0$  is the fluid density at  $T_0$ . The thermal buoyant force  $\mathbf{F}_B$  in the gravity field is

$$\mathbf{F}_B = -\rho_0 \mathbf{g} \beta (T - T_0), \tag{5}$$

where  $\mathbf{g}$  is the gravity acceleration. The characteristic length and velocity of the system are defined as the cavity length  $L$  and the lid-driven velocity  $U$ . Then the governing equation can be non-dimensionalized, yielding three dimensionless numbers, i.e., Prandtl number  $Pr$ , Reynolds number  $Re$ , and Grashof number  $Gr$ . They can be used to quantify the characteristics of the flow and heat transfer in the cavity system. The three dimensionless numbers are defined as

$$Pr = \nu / \alpha, \tag{6}$$

$$Re = UL / \nu, \tag{7}$$

$$Gr = g \beta (T_h - T_c) L^3 / \nu^2, \tag{8}$$

where  $g$  is the magnitude of  $\mathbf{g}$ . For simplicity, the Prandtl number  $Pr$  is set to 0.71 in this work.

### III. NUMERICAL METHODS

The double distribution function lattice Boltzmann model is used to solve the governing equations due to the better efficiency and accuracy in simulating the complex particulate two-phase flows with thermal convection.<sup>33,34</sup> According to Peng *et al.*,<sup>35</sup> the corresponding evolution equations of lattice Boltzmann model can be written as

$$f_i(\mathbf{r} + \mathbf{e}_i \delta_t, t + \delta_t) - f_i(\mathbf{r}, t) = -\frac{1}{\tau_f} [f_i(\mathbf{r}, t) - f_i^{eq}(\mathbf{r}, t)] + \delta_t F_i(\mathbf{r}, t), \tag{9}$$

$$g_i(\mathbf{r} + \mathbf{e}_i \delta_t, t + \delta_t) - g_i(\mathbf{r}, t) = -\frac{1}{\tau_g} [g_i(\mathbf{r}, t) - g_i^{eq}(\mathbf{r}, t)] + \delta_t Q_i(\mathbf{r}, t), \tag{10}$$

where  $f_i(\mathbf{r}, t)$  and  $g_i(\mathbf{r}, t)$  are the particle distribution function and thermal energy distribution function at the space position  $\mathbf{r}$  and time step  $t$ , respectively.  $\tau_f$  and  $\tau_g$  are the corresponding dimensionless relaxation time parameters, and  $f_i^{eq}(\mathbf{r}, t)$  and  $g_i^{eq}(\mathbf{r}, t)$  stand for the equilibrium distribution functions of  $f_i(\mathbf{r}, t)$  and  $g_i(\mathbf{r}, t)$ , respectively. The two-dimensional nine directions (D2Q9) model is adopted in this work, with the discrete velocity  $\mathbf{e}_i$  as

$$\mathbf{e}_i = \begin{cases} (0, 0), & i = 0, \\ c \left( \cos \left[ (i-1) \frac{\pi}{2} \right], \sin \left[ (i-1) \frac{\pi}{2} \right] \right), & i \in \{1, 2, 3, 4\}, \\ \sqrt{2} c \left( \cos \left[ (2i-1) \frac{\pi}{4} \right], \sin \left[ (2i-1) \frac{\pi}{4} \right] \right), & i \in \{5, 6, 7, 8\}, \end{cases} \tag{11}$$

where  $c$  is the lattice speed defined as the ratio of the lattice length  $\delta_x$  to time step  $\delta_t$ , which is selected as  $c = \delta_x / \delta_t = 1$ . The corresponding equilibrium distribution functions  $f_i^{eq}(\mathbf{r}, t)$  and  $g_i^{eq}(\mathbf{r}, t)$  are written as follows:<sup>35–37</sup>

$$f_i^{eq} = \begin{cases} -4d_0 \frac{p}{c^2} + \rho_f s_i(\mathbf{u}), & i = 0, \\ d_1 \frac{p}{c^2} + \rho_f s_i(\mathbf{u}), & i \in \{1, 2, 3, 4\}, \\ d_2 \frac{p}{c^2} + \rho_f s_i(\mathbf{u}), & i \in \{5, 6, 7, 8\}, \end{cases} \tag{12}$$

$$s_i(\mathbf{u}) = \omega_i \left[ 3 \frac{\mathbf{e}_i \cdot \mathbf{u}}{c^2} + 4.5 \frac{(\mathbf{e}_i \cdot \mathbf{u})^2}{c^4} - 1.5 \frac{\mathbf{u}^2}{c^2} \right],$$

$$g_i^{eq} = \begin{cases} \rho_f \omega_i T \left[ -\frac{3\mathbf{u}^2}{2c^2} \right], & i = 0, \\ \rho_f \omega_i T \left[ \frac{3}{2} + \frac{3\mathbf{e}_i \cdot \mathbf{u}}{2c^2} + \frac{9(\mathbf{e}_i \cdot \mathbf{u})^2}{2c^4} - \frac{3\mathbf{u}^2}{2c^2} \right], & i \in \{1, 2, 3, 4\}, \\ \rho_f \omega_i T \left[ 3 + 6 \frac{\mathbf{e}_i \cdot \mathbf{u}}{c^2} + \frac{9(\mathbf{e}_i \cdot \mathbf{u})^2}{2c^4} - \frac{3\mathbf{u}^2}{2c^2} \right], & i \in \{5, 6, 7, 8\}, \end{cases} \tag{13}$$

where the weight coefficient  $\omega_i$  is written as  $\omega_0 = 4/9$ ,  $\omega_{1-4} = 1/9$ , and  $\omega_{5-9} = 1/36$ . The parameters  $d_0$ ,  $d_1$ , and  $d_2$  are chosen as  $d_0 = 5/12$ ,  $d_1 = 1/3$ , and  $d_2 = 1/12$ , respectively. The discrete forcing term  $F_i(\mathbf{r}, t)$  and the discrete heat source term  $Q_i(\mathbf{r}, t)$  exerted on the fluid flow are given by

$$F_i(\mathbf{r}, t) = \left(1 - \frac{1}{2\tau_f}\right) \omega_i \left[3 \frac{\mathbf{e}_i - \mathbf{u}}{c^2} + 9 \frac{\mathbf{e}_i \cdot \mathbf{u}}{c^4} \mathbf{e}_i\right] \cdot \mathbf{F}, \quad (14)$$

$$Q_i(\mathbf{r}, t) = \left(1 - \frac{1}{2\tau_g}\right) \omega_i Q, \quad (15)$$

where  $\mathbf{F}$  is the total body force term and  $Q$  is the heat generation term.<sup>38</sup> The macroscopic velocity  $\mathbf{u}$ , pressure  $p$ , and temperature  $T$  of fluid flow can be calculated by

$$\rho_f \mathbf{u} = \sum_{i=1}^8 c \mathbf{e}_i f_i + \frac{\delta_t}{2} \mathbf{F}, \quad (16)$$

$$p = \rho_f \frac{c^2}{4d_0} \left[\sum_{i=1}^8 f_i + s_0(\mathbf{u})\right], \quad (17)$$

$$\rho_f T = \sum_{i=0}^8 g_i + \frac{\delta_t}{2} Q. \quad (18)$$

The incompressible Navier–Stokes equations can be recovered through the Chapman–Enskog expansion analysis,<sup>35,43</sup> and then, the kinematic viscosity  $\nu$  and the thermal diffusivity  $\alpha$  can be related to the dimensionless relaxation time parameters  $\tau_f$  and  $\tau_g$  as

$$\nu = (2\tau_f - 1)/6, \quad (19)$$

$$\alpha = (2\tau_g - 1)/3. \quad (20)$$

The non-equilibrium extrapolation boundary scheme<sup>39</sup> is implemented to determine the unknown variables on the cavity walls. For the complex moving boundary of the particle, the immersed boundary method (IBM)<sup>40,41</sup> is adopted. The particle boundary is treated as a series of Lagrangian points that immersed in the fluid, where the interactions between the fluid flow and the particle boundary are imposed as the source terms.<sup>42</sup> The external body force term and heat generation term exerted on the Eulerian fluid nodes  $F_b(\mathbf{r}, t)$  and  $Q_b(\mathbf{r}, t)$  can be calculated by

$$F_b(\mathbf{r}, t) = \sum_r f_b D(\mathbf{r} - \mathbf{X}_b(s, t)) \Delta s, \quad (21)$$

$$Q_b(\mathbf{r}, t) = \sum_r q_b D(\mathbf{r} - \mathbf{X}_b(s, t)) \Delta s, \quad (22)$$

where  $f_b$  and  $q_b$  are the force density and heat source density on the Lagrange point  $\mathbf{X}_b$  located at coordinate  $s$  on the boundary curve  $\Gamma$ , respectively, and  $\Delta s$  is the arc corresponding to the Lagrange point. Note that the external force density is added into the total body force term  $\mathbf{F}$  in treating the particle boundary in the IBM. The effects of  $f_b$  and  $q_b$  are diffused to the Eulerian fluid nodes through the discrete delta function  $D(\mathbf{x})$ . Here, the delta function in cosine-format is considered,<sup>41</sup>

$$D(\mathbf{r} - \mathbf{X}_b) = \delta(x - x_b) \delta(y - y_b),$$

$$\delta(m) = \begin{cases} \frac{1}{4} \left(1 + \cos\left(\frac{\pi|m|}{2}\right)\right), & |m| \leq 2, \\ 0, & |m| > 2, \end{cases} \quad (23)$$

where  $x_b$  and  $y_b$  are the coordinates of Lagrange point  $\mathbf{X}_b$ , while  $x$  and  $y$  are the coordinates of the Eulerian fluid node. Moreover, in order to

achieve the no-slip and constant temperature boundary condition on the particle surface, a direct-force scheme that has no free parameters is implemented for calculating  $f_b$  and  $q_b$ ,<sup>33</sup> based on the split force scheme of LBM<sup>43</sup>

$$f_b = 2\rho_f \frac{U_b - \mathbf{u}_b^{\text{noF}}}{\delta t}, \quad (24)$$

$$\mathbf{u}_b^{\text{noF}} = \sum_r \mathbf{u}_r^{\text{noF}} D(\mathbf{r} - \mathbf{X}_b) \delta_x^2,$$

$$q_b = 2\rho_f \frac{T_b - T_b^{\text{noE}}}{\delta t}, \quad (25)$$

$$\rho_f T_b^{\text{noE}} = \sum_r \rho_f T_r^{\text{noE}} D(\mathbf{r} - \mathbf{X}_b) \delta_x^2,$$

where  $\mathbf{u}_b^{\text{noF}}$  and  $T_b^{\text{noE}}$  are the macroscopic velocity and temperature of the fluid flow without imposing the external force and heat source generated by the particle, which are obtained by those on the Eulerian fluid node through the distribution function  $D$ .  $U_b$  and  $T_b$  are the desired velocity and temperature on the particle surface

$$U_b = V_p + \omega_p \times (\mathbf{X}_b - \mathbf{X}_p), \quad T_b = T_c, \quad (26)$$

where  $V_p$  and  $\omega_p$  are the translational and rotational velocity of the particle, respectively, while  $\mathbf{X}_b - \mathbf{X}_p$  is the position vector of  $\mathbf{X}_b$  on the particle surface based on the particle center.

Since  $f_b$  and  $q_b$  are available, the evolution of flow field can be propelled. As to the particle, the interaction of fluid flow can be calculated as follows:

$$\mathbf{F}_p = \sum_r f_b \Delta s, \quad \mathbf{T}_p = \sum_r (\mathbf{X}_b - \mathbf{X}_p) \times f_b \Delta s, \quad (27)$$

where  $\mathbf{F}_p$  and  $\mathbf{T}_p$  are the total force and torque exerted on the particle, respectively. Hence, the particle motion can be solved through Newton’s law of motion

$$\frac{dV_p}{dt} = \frac{1}{M_p} \mathbf{F}_p + \frac{1}{M_p} \mathbf{F}_w, \quad \frac{d\omega_p}{dt} = \frac{1}{I_p} \mathbf{T}_p, \quad (28)$$

where  $M_p$  is the total mass of the particle,  $I_p$  is the rotational inertia of the particle, and  $\mathbf{F}_w$  is introduced to deal with the collision between the particle and cavity wall<sup>44,45</sup> and modeled as

$$\mathbf{F}_w = \begin{cases} \frac{k}{\varepsilon} \left(\frac{\|\mathbf{w}\| - 2R - \xi}{\xi}\right)^2 \frac{\mathbf{w}}{\|\mathbf{w}\|}, & \|\mathbf{w}\| \leq 2R + \xi, \\ 0, & \|\mathbf{w}\| > 2R + \xi, \end{cases} \quad (29)$$

where  $\mathbf{w} = 2(\mathbf{X}_p - \mathbf{X}_w)$  is the vector along the distance between the particle and cavity wall,  $\mathbf{X}_w$  is the foot point on the wall,  $R$  is the radius of the particle, and  $k$  and  $\varepsilon$  are the force scale factor and stiffness scale factor, respectively.  $\mathbf{F}_w$  is applied once the gap between the particle and the cavity wall is less than the threshold  $\xi$ , which is set as one grid size in the present work.

#### IV. MODEL VALIDATION

In order to validate the in-house code based on the numerical methods, the settling of a circular cold particle in a channel is first checked. The results are compared with several previous studies.<sup>26,46</sup> In the validation, the vertical channel is filled with the hot fluid of temperature  $T_h = 1$ , density  $\rho_f = 1$ , and Prandtl number  $Pr = 0.7$ , while the temperature of boundary walls is also kept at  $T_h = 1$ . The no-slip boundary conditions are adopted for the walls. The width  $W$  and



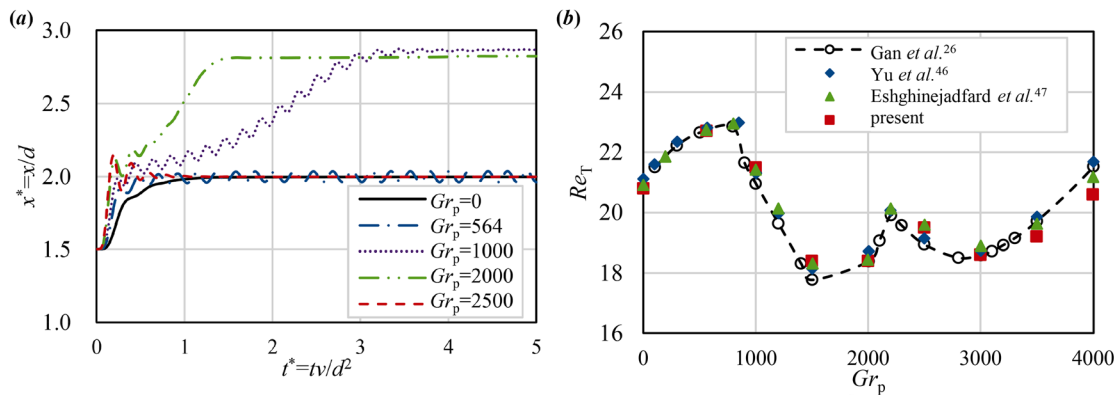


**FIG. 2.** The result for the cold particle settling in hot fluid: (a) the lateral trajectories of the particle for various particle Grashof number  $Gr_p$  and (b) the terminal particle Reynolds number  $Re_T$  for various  $Gr_p$ .

height  $H$  of the computational domain are set as  $W = 4d_p$  and  $H = 160d_p$ , respectively, where  $d_p$  is the particle diameter which is resolved by 50 grids. The circular particle with the density  $\rho_p = 1.00232$  and the constant surface temperature  $T_c = 0$  is initially released at  $0.5d_p$  away from the centerline of channel. The particle Reynolds number is defined as  $Re_p = U_{ref}d_p/\nu$  and the reference value of  $Re_p$  is 40.5 according to Yu *et al.*,<sup>46</sup> where the reference velocity  $U_{ref}$  is defined as  $U_{ref} = \sqrt{\pi d_p/2(\rho_p/\rho_f - 1)g}$  and the dimensionless relaxation time  $\tau_f = 3\nu + 0.5$  is set at 0.65. The particle's Grashof number  $Gr_p = g\beta(T_h - T_c)d_p^3/\nu^2$  at the range of  $0 \leq Gr_p \leq 4000$  is applied. The results of particle motion after it is released from the initial position are shown in Fig. 2 and Table I. Gan *et al.*<sup>26</sup> and Yu *et al.*<sup>46</sup> studied the motion of particle during sedimentation and found that it is dependent upon the particle Grashof number. Our numerical results replicate the motion behaviors during the sedimentation. As shown in Fig. 2(a), for either lower  $Gr_p$  (e.g.,  $Gr_p = 564$ ) or higher  $Gr_p$  (e.g.,  $Gr_p = 2500$ ), the particle settles along the centerline or laterally oscillates along it. However, for  $Gr_p$  in between (e.g.,  $Gr_p = 1000$ ), the particle tends to equilibrate at the vertical track deviating from the centerline. The sedimentation of the particle exhibits several types of trajectories in the corresponding  $Gr_p$  regime, which is consistent with the previous work.<sup>26,46</sup> The terminal Reynolds numbers  $Re_T$  of the particle at various  $Gr_p$  also agree well with the results in previous reports,<sup>26,46,47</sup> according to Fig. 2(b). Furthermore, the equilibrium positions for  $Gr_p = 1000$  and 2000 are indicated in Table I, which also align well with the results in the literature. Hence, the numerical methods can be well used to solve the fluid-particle interaction in the presence of thermal convection.

**TABLE I.** The equilibrium positions for the settling particle when  $Gr_p$  is 1000 and 2000.

$Gr_p$	Present	Yu <i>et al.</i> <sup>46</sup>	Yang <i>et al.</i> <sup>27</sup>	Hu and Guo <sup>28</sup>
1000	2.87	2.89	2.89	2.91
2000	2.82	2.74	2.79	2.76

**V. RESULTS AND DISCUSSION**

**A. Grid independence validation**

The grid independence validation is studied to ensure the accuracy of the numerical method when treating the problem with the different mesh sizes. Three grid sizes of  $750 \times 750$ ,  $1000 \times 1000$ , and  $1250 \times 1250$  are implemented, which represent the cavity length  $L = 750, 1000, 1250$ , respectively. Then the neutrally buoyant particle with the diameter  $d_p$  is released at  $(0.25L, 0.25L)$  in the cavity at  $Re = 1000$  and  $Gr = 2 \times 10^5$ . According to Fig. 3, the results show that the computed trajectories of the particle for various grid sizes are consistent. Thus,  $L = 1000$  is chosen for saving computing resources and time in this work. Here, the results of the particle trajectories and velocity are non-dimensionalized with the cavity length  $L$  and lid-driven velocity  $U$ . Moreover, it can be observed that the particle moves along a certain trajectory in the periphery of cavity and shows a stable periodic motion after an initial stage. However, the trajectory is not the same as the centrosymmetric limit cycle reported in the isothermal cases,<sup>21</sup> due to the thermal convection in the cavity flow. Hence, with the effects of fluid inertia and buoyancy, the dynamics of particle motion in the non-isothermal cavity flow remains unclear. Therefore, the effects of cavity Grashof number and Reynolds number

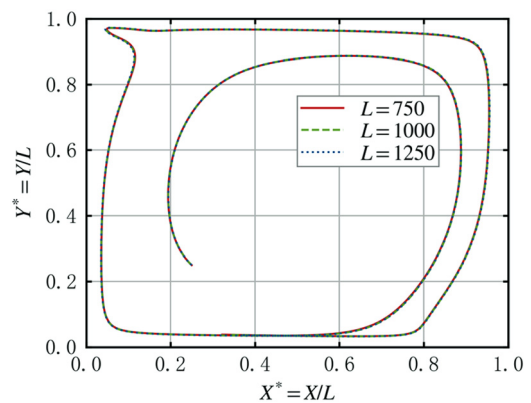


**FIG. 3.** The trajectories of a neutrally buoyant cold particle in thermal two-sided lid-driven cavity flow for various grid sizes  $L$ . ( $Re, Gr, d_p/L = (1000, 2 \times 10^5, 0.05)$ ).

19 December 2023 11:19:46

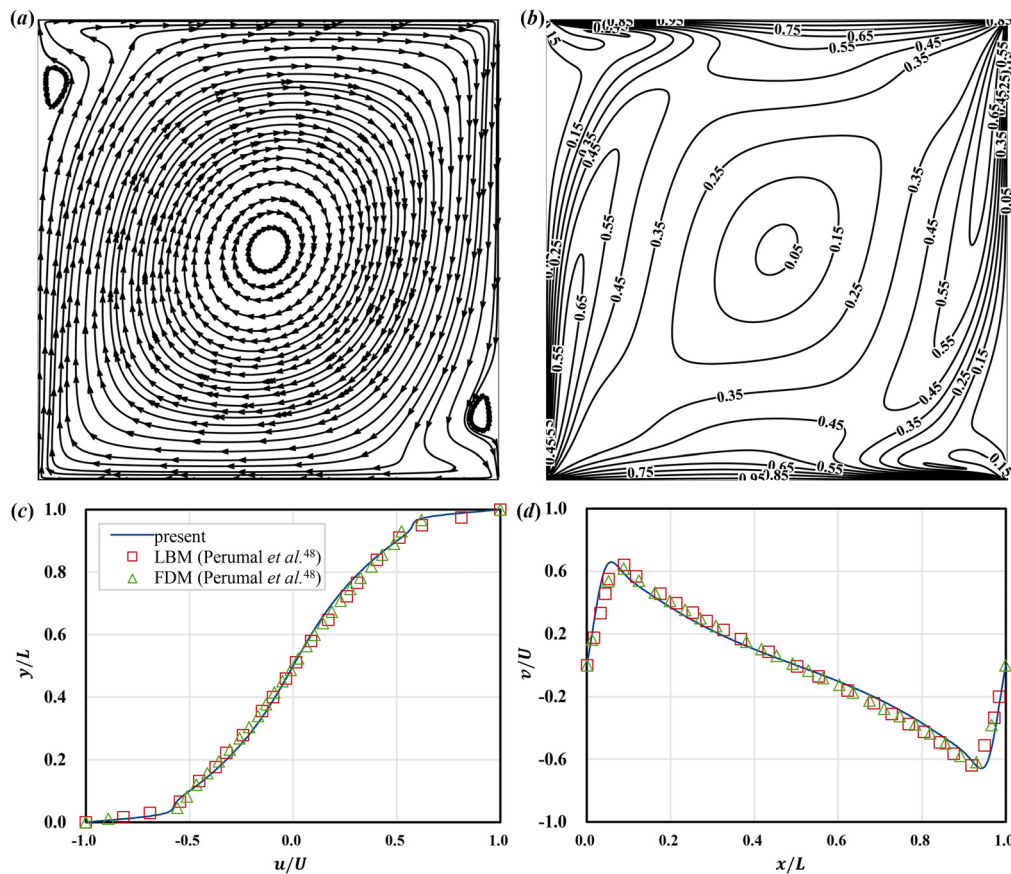


FIG. 4. The background flow field of two-sided lid-driven flow for  $Re = 1000$ : (a) the streamlines; (b) the contours of normalized fluid speed  $|u|/U_{ref}$ ; (c) the horizontal velocity profile along  $x/L = 0.5$ ; and (d) the vertical velocity profile along  $y/L = 0.5$ .

on the particle trajectory and the corresponding flow pattern are discussed in the following.

### B. Effect of Grashof number

The neutrally buoyant particle of diameter  $d_p = 0.05L$  is released in the cavity flow with  $Re = 1000$  from the initial position  $(0.25L, 0.25L)$  following Hu *et al.*<sup>21</sup> The steady two-sided lid-driven cavity flow is obtained in advance, to avoid the initial flow transient as it could affect the particle motion and decay the emerge of steady state.<sup>19</sup> In addition, for the better understanding of the particle motion in the cavity flow, the streamlines and velocity contours of two-sided lid-driven flow at  $Re = 1000$  in steady state are illustrated in Figs. 4(a) and 4(b). According to Fig. 4(a), the central symmetric flow forms two corner eddies, swirling anticlockwise in the top-left and bottom-right corners of the cavity, respectively. The primary eddy structure is located at the center of the cavity, which swirls in a clockwise direction. In addition, the velocity contours in Fig. 4(b) show the presence of high velocity gradients near the cavity wall, and the low fluid speeds emerge at the center and corner regions of the cavity. The comparison of the velocities along the centerline [as shown in Figs. 4(c) and 4(d)] to those by Perumal *et al.*<sup>48</sup>

demonstrates that our results recur the flow pattern of the two-sided lid-driven cavity flows.

Then, the particle motion in the two-sided lid-driven cavity is investigated for various  $Gr = 10^4 - 10^7$  at  $Re = 1000$ . Figure 5 shows

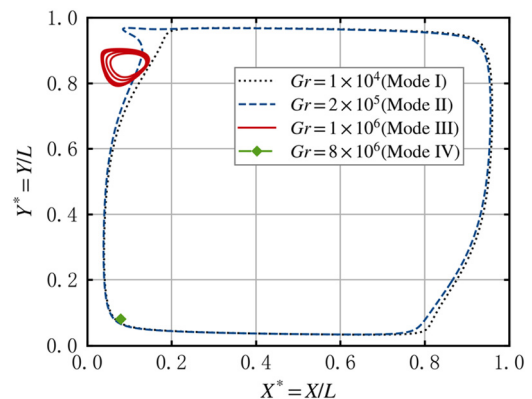


FIG. 5. The four modes of particle motion in steady state for various Grashof number  $Gr$ . Here the particle size  $d_p = 0.05L$  and the cavity Reynolds number  $Re = 1000$ .

the effects of  $Gr$  on the particle motion in the cavity. It is noted that the particle moves periodically along the fixed orbit after the initial transient phase, and the particle motion can be classified into four modes. To be specific, in mode I (for  $Gr < 5 \times 10^4$ ) the orbit that the particle moves along is in the periphery of cavity, demonstrating a nearly central symmetry. In mode II (for  $Gr$  at  $5 \times 10^4 - 3 \times 10^5$ ), the centrosymmetry of the particle trajectory is broken and the particle shows an orbit deformation in the top-left corner of the cavity. In mode III (for  $Gr$  at  $3 \times 10^5 - 1.5 \times 10^6$ ), the orbit shrinks and is located in the top-left corner of the cavity. In mode IV (for  $Gr$  over  $1.5 \times 10^6$ ), the orbit migrates to the bottom-left of the cavity. In order to further understand the physics underlying these four modes, detailed analysis and discussion are presented in the following.

1. Mode I

In mode I, the centrosymmetric orbit is observed, which could be considered as the emergence of the limit cycle alike phenomenon of the particle motion, similar to the isothermal states in the absence of buoyancy effect ( $Gr = 0$ ).<sup>21</sup> To illustrate the buoyancy effect, the particle motion is studied for  $Gr = 10^4$ , which is further compared with the case of forced convection (i.e.,  $Gr = 0$ ). As shown in Fig. 6, it can be seen that the trajectory of the particle for  $Gr = 10^4$  at the steady state is similar to that of the particle for  $Gr = 0$ , which indicates that the buoyancy effect is still weak for these cases, resulting in the negligible influence on the heat and momentum exchange between the particle and fluid flow. Therefore, mode I represents the minor buoyancy effect on the particle motion with the low  $Gr$ . In this mode, the particle motion is dominated by the interaction between centrifugation in the circulating flow and the repulsion of cavity wall,<sup>16,18</sup> demonstrating the similar centrosymmetric orbit as in the isothermal cases.

2. Mode II

As shown in Fig. 7, the trajectory of the particle in the steady state gradually deforms with the increase in  $Gr$ , which presents the transition of particle motion mode from mode I to mode II. The gradually enhanced asymmetry of the trajectory is observed in mode II, as the deformation in the top-left corner shows. This indicates the different

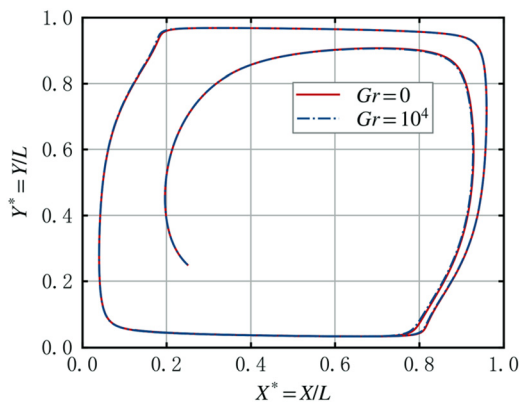


FIG. 6. The trajectories of the particle starting from  $t^* = tU/L = 0$  in two-sided lid-driven cavity flow, for  $Gr = 0$  or  $Gr = 1 \times 10^4$ , and  $Re = 1000$ .

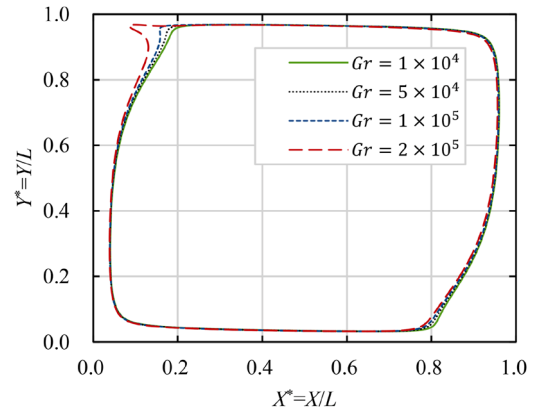


FIG. 7. The trajectory of the neutrally buoyant cold particle at steady state in the thermal two-sided lid-driven cavity flow with various  $Gr$  for  $Re = 1000$ .

hydrodynamic forces exerted on the particle due to the gradually increased buoyancy effect.

In order to further investigate the physics underlying particle motion in mode II, the speed and trajectories of the particle in both  $x$ - and  $y$ -direction from the initial transient phase at  $Gr = 2 \times 10^5$  are discussed in detail. As shown in Fig. 8, the particle is sharply accelerated and moves with the cavity flow, finally approaching the steady

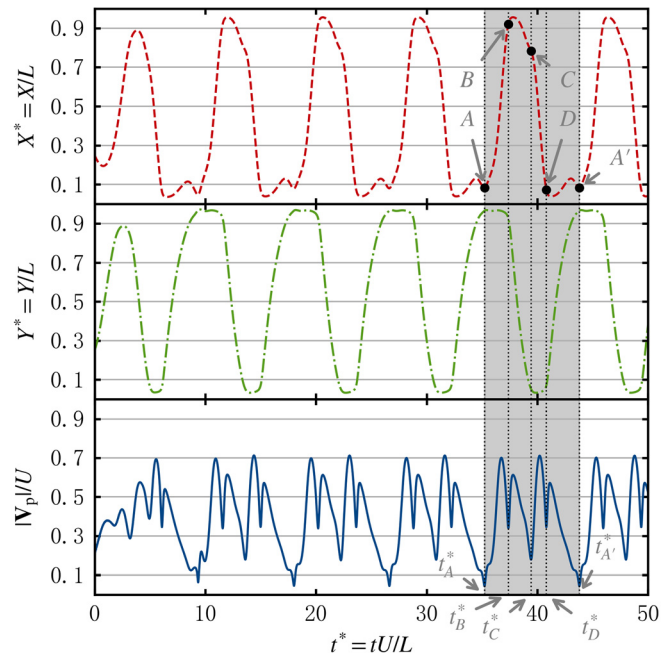


FIG. 8. The process of the particle motion for  $Gr = 2 \times 10^5$  and  $Re = 1000$ . The solid, dashed-dotted, and dash lines from bottom to top subgraph represent normalized speed as well as the trajectories in  $y$ - and  $x$ -direction, respectively. The filled area from  $A$  to  $A'$  is one period for the particle moving along the orbit, and the points are annotated when the local minimal value of speed arises. The corresponding dimensionless times of four locations  $A$ ,  $B$ ,  $C$ , and  $D$  are:  $t_A^* = 35.230$ ;  $t_B^* = 37.385$ ;  $t_C^* = 39.440$ ;  $t_D^* = 40.815$ ; and  $t_{A'}^* = 43.800$ .



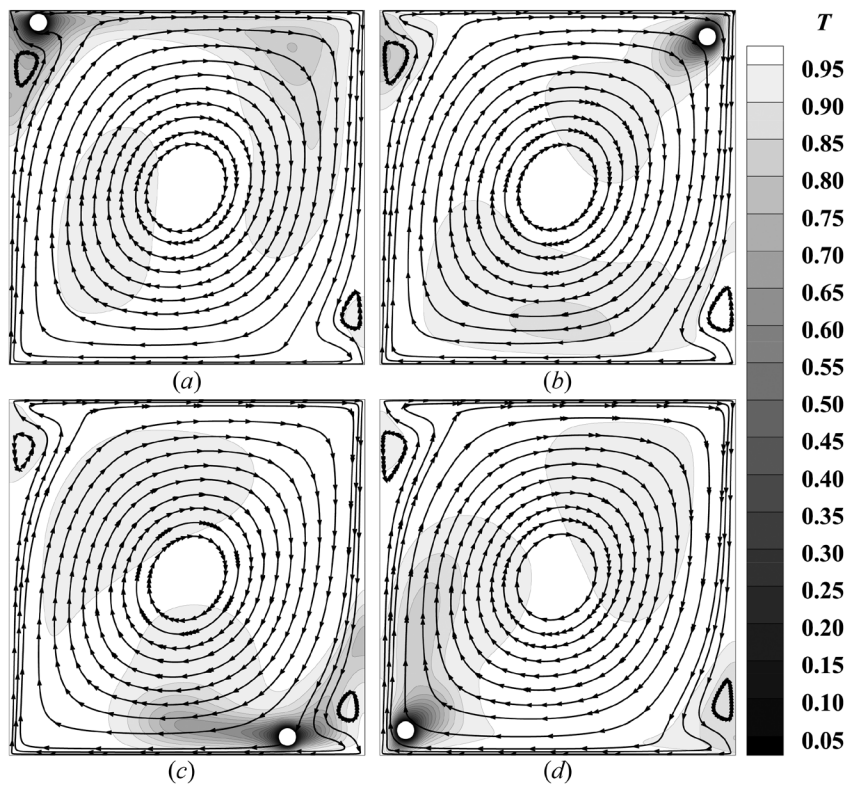


FIG. 9. The snapshots of streamlines and isotherms and particle position in the cavity flow at: (a)  $t^* = t_A^*$ ; (b)  $t^* = t_B^*$ ; (c)  $t^* = t_C^*$ ; and (d)  $t^* = t_D^*$ .

orbit. In the steady state, both the periodic trajectories and the evolutions of particle speed could be observed. The shadow zone of Fig. 8 shows a typical single period of particle motion at the steady state. The corresponding coordinates and speed show the clockwise movement of the particle, i.e., the particle moves along the trajectory of  $ABCD$ . Note that the points are located at the top-left corner  $A$ , the top-right corner  $B$ , the bottom-right corner  $C$ , and the bottom-left corner  $D$  of the cavity, respectively. After that, the particle returns to the top-left corner of the cavity at the point  $A'$ . As can be observed, the speed of the particle lowers down when it approaches the wall corner. This can be ascribed to the lubrication force exerted on the particle in the cavity corners, which will be further enhanced with the decrease in lubrication gap between the particle and boundary wall and annihilate part of the kinetic energy of the particle.<sup>16,18</sup> Thus, the particle velocity is suppressed by the confinement effects of walls in the cavity corners. Moreover, the corresponding snapshots of flow fields and isotherms when the particle inhabits  $A$ ,  $B$ ,  $C$ , and  $D$  are shown in Fig. 9. Since the two corner eddies exist in the top-left corner and bottom-right corner of the cavity, according to Fig. 4, the lower velocity of the fluid flow could further decrease the speed of the particle in the nearby. Hence, the particle speed is lower at  $A$  and  $C$  than at  $B$  and  $D$ . Furthermore, since the presence of particle reduces the temperature of the surrounding fluid flow, the thermal buoyant force exerted on the fluid flow is constantly negative along  $y$ -direction.<sup>28,30,31</sup> Then, the buoyancy effect slows down the particle speed when the particle is around  $A$ , but increases the particle speed when the particle moves around  $C$ . This results in the lower speed of the particle at  $A$  compared to at  $C$ . Hence, the particle has a longer residence time at the top-left corner.

Moreover, the longer residence time of the particle at the cavity corners would enhance the heat exchange between fluid and particle, which further enhances the buoyancy effect. Therefore, in model II the trajectory of the particle deforms prominently in the top-left corner of the cavity, compared to that in the mode I.

### 3. Mode III

Figure 10 shows the process of particle migration from the initial position to the top-left corner of the cavity at  $Gr = 10^6$  and  $Re = 1000$ . As shown in Fig. 10(a), the particle moves clockwise along the primary eddy and then enters the corner eddy in the top-left region. After that, the particle performs an anticlockwise translational motion following the orientation of the corner eddy. Moreover, the velocities of the particle oscillate around zero after the initial transient stage according to Fig. 10(b), demonstrating a nearly circular track of the particle in the top-left corner in the cavity. The positive angular velocity corresponds to the anticlockwise rotation of the particle, while the angular velocity demonstrates a quasi-periodic pattern, indicating that the particle motion of mode III is not a strict steady state. Figure 11 shows the instantaneous fluid flow and temperature field after the particle enters the top-left corner of the cavity. It can be seen that the corner eddy containing the particle deforms significantly, while the rest part of the cavity flow maintains the original streamlines and isotherms pattern. In this case, the particle motion can be considered as the evolution of mode II. As  $Gr$  increases, the buoyancy effect is further enhanced when the particle passes the top-left corner of cavity. Thus, the deformation of the corner eddy is promoted, further

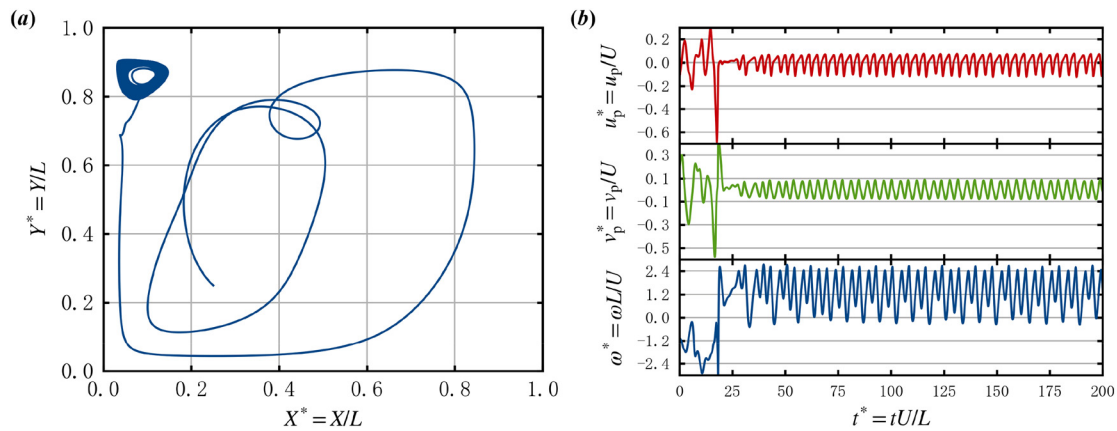


FIG. 10. The trajectories of the particle for  $Gr = 10^6$  and  $Re = 1000$ : (a) the motion trail in the cavity and (b) the time histories of particle angular velocity and velocities.

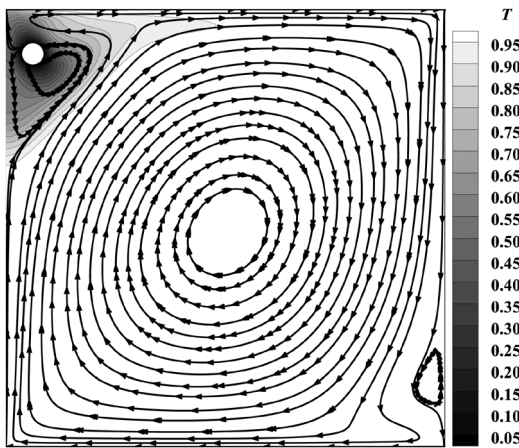


FIG. 11. The instantaneous streamlines and isotherms for particle moving in the two-sided lid-driven cavity flow with  $Gr = 10^6$  and  $Re = 1000$  at  $t^* = 200$ .

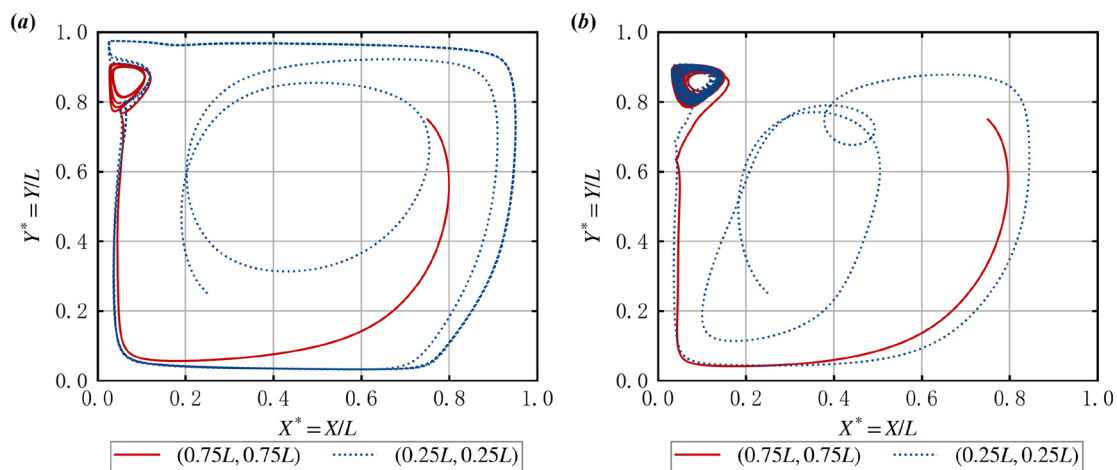
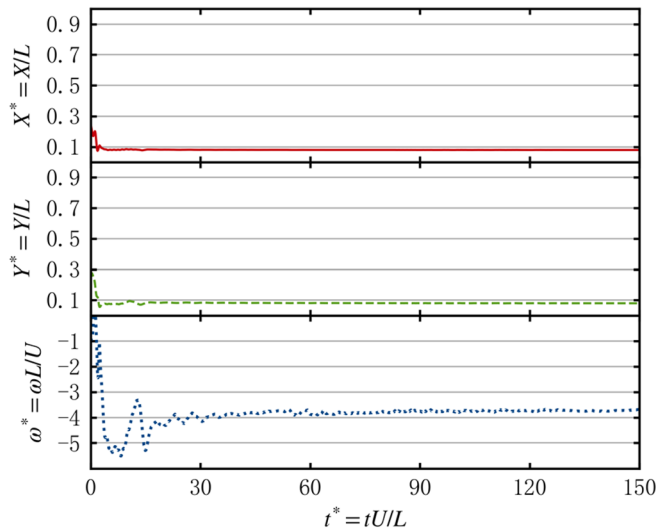


FIG. 12. The trajectory of neutrally buoyant cold particle initially released at  $(0.75L, 0.75L)$  and  $(0.25L, 0.25L)$  in the thermal two-sided lid-driven cavity flow for  $Re = 1000$  and (a)  $Gr = 5 \times 10^5$  and (b)  $Gr = 10^6$ .

impeding the particle from passing through the region. In other words, the particle can be easily captured by the corner eddy in the top-left corner. If the cold particle is entrapped, a low-temperature zone would be formed in the corner region.

One exception case is for  $Gr = 5 \times 10^5$ , in which an orbit in the periphery of the cavity with the significant deformation in the top-left corner appears. This is similar to the particle motion of mode II [according to the dot line in Fig. 12(a)]. However, for either a lower  $Gr = 4 \times 10^5$  or a higher  $Gr = 6 \times 10^5$ , the particle motion behavior of typical mode III can be observed. According to Liu *et al.*,<sup>30</sup> this could be due to the initial setting position of the particle in the cavity. To further understand the transition of the particle motion mode, the trajectories of the particle with the different initial positions and different  $Gr$  are shown in Fig. 12. For  $Re = 1000$  and  $Gr = 5 \times 10^5$ , as can be seen, when the particle is initially placed at the position of  $(0.25L, 0.25L)$ , a final steady mode II motion can be reached. While the particle is initially placed at  $(0.75L, 0.75L)$ , a final steady mode III motion can be obtained, as shown in Fig. 12(a). However, the two initial positions lead to the same particle motion mode of mode III for



**FIG. 13.** The time history of particle motion for  $Gr = 8 \times 10^6$  and  $Re = 1000$ . The dotted, dash, and solid lines from bottom to top subgraph represent normalized rotational velocity as well as the trajectories in  $y$ - and  $x$ -direction, respectively.

$Re = 1000$  and  $Gr = 10^6$ , as shown in Fig. 12(b). The results suggest that the motion mode of the particle could be affected by the particle initial position, for the cases that approach to the critical  $Gr$  for transitions of motion mode. The different initial states cause the different initial transient phases of the particle, and thus, the velocity of the particle when the particle passes through the top-left corner should be different. Then, the particle at the specific  $Gr$  and  $Re$  might not certainly enter mode III. In this context, the particle motion is determined by the combination of buoyancy effect and inertia, and the combination determines whether the particle will enter the corner eddy and is unable to drop out. Thus, the motion mode of the particle could show instability.

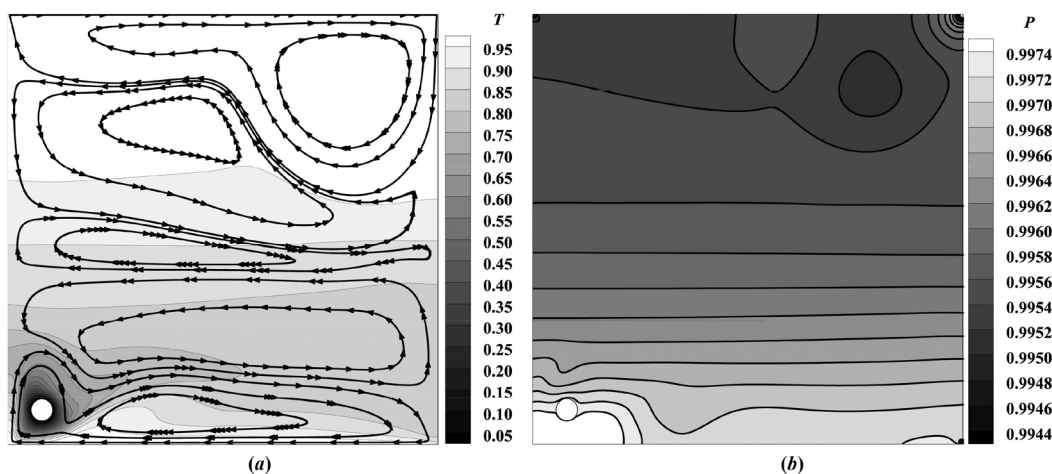


**FIG. 14.** The snapshot at  $t^* = 150$  of particle moving in the two-sided lid-driven cavity flow for  $Gr = 8 \times 10^6$  and  $Re = 1000$ : (a) the streamlines and isotherms and (b) the pressure contours.

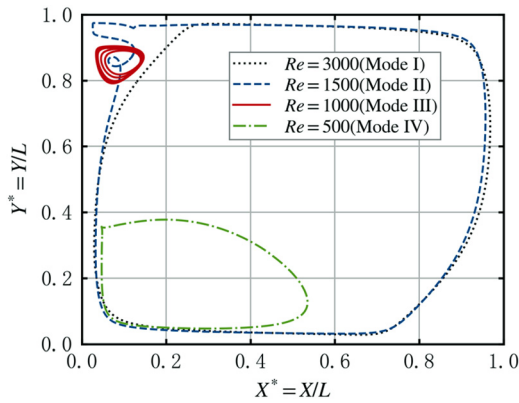
#### 4. Mode IV

Figure 13 shows the trajectories and rotational angular velocities of the particle from the initial state at  $Gr = 8 \times 10^6$  and  $Re = 1000$ . The particle eventually suspends in the bottom-left corner of the cavity at a fixed point and rotates clockwise with a constant angular velocity. To further understand the mechanism of the phenomenon, the flow field is depicted in Fig. 14. The streamlines and isotherms in Fig. 14(a) demonstrate a stable stratification of the cavity flow. The fluid flow circuits in the fluid layers that distribute along the vertical direction in the cavity, and the particle suspends in the bottom layer, which can cause the low-temperature zone to develop in the lower part of cavity. Then the vertical distribution of isotherms can be observed because of the effect of thermal convection. Such flow pattern indicates the dominant buoyancy-driven natural convection compared to the lid-driven forced convection, since the  $Gr$  is much larger than  $Re$ , and this is also supported by Iwatsu *et al.*<sup>49</sup> In addition, the dimensionless pressure field of cavity flow also emerges a stratification state as shown in Fig. 14(b). It can be seen that the pressure at left and right sides of the particle shows equivalence, but the pressure at the bottom of the particle is higher than that at the top of the particle. Therefore, an upward hydrodynamic force exerted on the particle can be caused by the pressure difference. Thus, the particle is able to suspend on the fixed position in the bottom-left corner of cavity due to the interaction between the downward thermal effect and upward hydrodynamic force.

#### C. Effect of Reynolds number

Since the fluid inertia plays a significant role in the particle motion, the effects of cavity Reynolds number on the motion of particle are further studied. The neutrally buoyant cold particle with a diameter of  $d_p = 0.05L$  is released from the same position of  $(0.25L, 0.25L)$  in the cavity filled with the hot fluid flow. Figure 15 shows the particle orbits at the steady states within the Reynolds number range of  $500 \leq Re \leq 3000$  at a constant Grashof number of  $10^6$ . It presents that the particle in the steady state performs the similar motion behaviors to the cases for various  $Gr$  and fixed  $Re$  (as shown in Fig. 5).





**FIG. 15.** The trajectories of the particle at the steady state for various Reynolds number  $Re$  with  $d_p = 0.05L$  and  $Gr = 10^6$ .

First, for the high  $Re$  case ( $Re = 3000$ ), the limit cycle-like orbit can be observed, indicating the characteristics of mode I. For the lower Reynolds number  $Re = 1500$ , the trajectory remains similar with the case  $Re = 3000$ , except the deformation of the top-left corner portion. Such motion behavior can be categorized as mode II. Upon a further decrease in the Reynolds number to  $Re = 1000$ , the motion behavior of the particle exhibits the feature of mode III, i.e., the ring-shape-orbit motion of the particle emerges in the top-left corner of the cavity. Finally, for  $Re = 500$ , the steady orbit of the particle migrates to the bottom-left area of the cavity. Although the ring-shape orbit arises instead of a fixed point, it can also be classified as mode IV, which will

be further discussed next. The evolution of particle motion modes reemerges for the different  $Re$  at the fixed  $Gr$ , and this demonstrates that the Reynolds number is also the important parameter that effects the transition of particle motion mode.

To gain a better understanding of the flow patterns and temperature field in the cavity, Fig. 16 presents the four corresponding snapshots of the particle in the cavity flow for the four cases depicted in Fig. 15. For  $Re = 3000$  according to Fig. 16(a), the particle passes by the top-left corner, but it is unable to enter the corner eddy. The thermal convection causes the low-temperature fluid flow around the particle in the primary eddy of the cavity flow. This indicates that the lid-driven forced convection is dominant in the system, and thus the influences of the particle and thermal convection on the flow pattern and temperature of the corner eddies are minimal. Moreover, Fig. 16(b) shows that for  $Re = 1500$ , the particle temporarily enters the corner eddy. The low-temperature zone exhibits a tendency to converge in the top-left corner of the cavity rather than the area of primary eddy. Comparing the case of  $Re = 1500$  to the case of  $Re = 1000$  as shown in Fig. 16(c), the further developing corner eddy in the bottom-right corner for  $Re = 1500$  indicates the higher inertia effect. However, the corner eddies on the top-left corner at  $Re = 1000$  and  $1500$  show the similar sizes, and this indicates the relatively low buoyancy effect for  $Re = 1500$ . Finally, the snapshot at  $Re = 500$  depicts that the primary eddy of the cavity flow is split into the upper and the lower parts; meanwhile, the low-temperature zone mainly exists in the lower one following the particle, as shown in Fig. 16(d). Although such motion behavior is not observed for the cases of  $Re = 1000$  with various  $Gr$  in Sec. V B, it also can be classified as mode IV. This classification is justified by the similarity in the characteristics of fluid and temperature

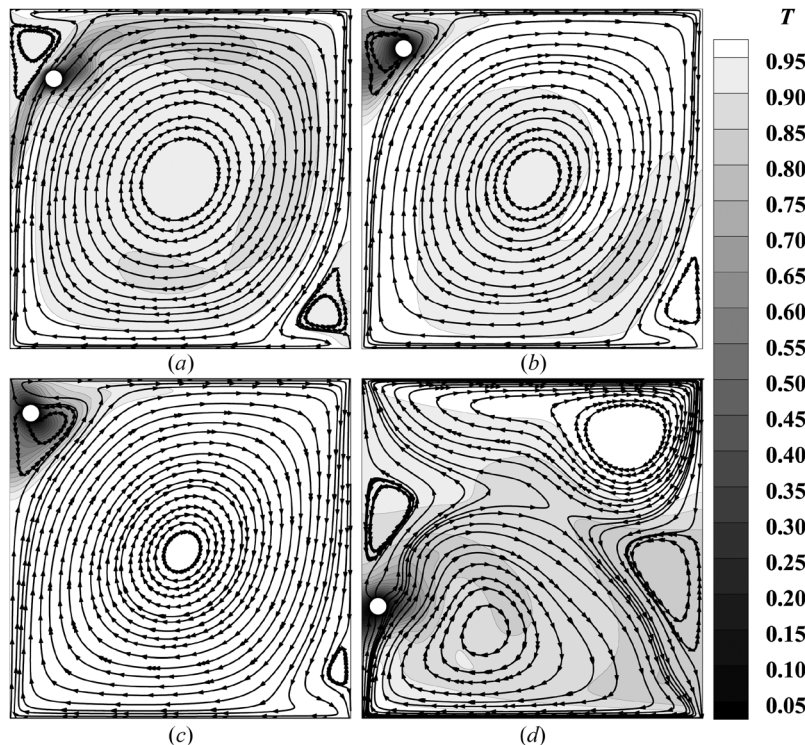


**FIG. 16.** The instantaneous streamlines and temperature contours of the particle moving in the two-sided lid-driven cavity flow for  $Gr = 10^6$ : (a)  $t^* = 175$  for  $Re = 3000$  (mode IV); (b)  $t^* = 175$  for  $Re = 1500$  (mode III); (c)  $t^* = 200$  for  $Re = 1000$  (mode II); and (d)  $t^* = tU/L = 200$  for  $Re = 500$  (mode I).

fields with the significantly higher  $Gr$  than  $Re$ . The reason that the particle does not perform the motion on the fixed point might attribute to the low  $Gr$ , and then the relatively higher lid-driven forced convection effect leads the particle to undergo the periodic motion along the steady orbit. On the other hand, the fix-point motion can also be treated as the periodic motion with the negligible time period and size of steady orbit.

**D. The transition of particle motion mode with  $Gr$  and  $Re$**

As discussed above, the motion modes of the particle in the cavity could be caused by the combined effect of the lid-driven forced convection ( $Re$ ) and buoyancy-driven natural convection ( $Gr$ ). The forced convection would lead the particle to move along the limit-cycle alike orbit, while the natural convection could cause the deviation from the orbit. To further understand the mechanism underlying the transition of particle motion in the cavity, we simulated the particle motion for  $Re = 500-3000$  and  $Gr = 10^4-10^7$ . Note that the cases of  $Gr < 10^4$  are not considered since a low Grashof number has negligible influence on the motion of particle. In the simulations, the particle with  $d_p = 0.05L$  is released from the same position  $(0.25L, 0.25L)$  in the cavity.

A diagram of particle motion in cavity flow for the various  $Re$  and  $Gr$  is shown in Fig. 17. It can be observed that in general the motion mode of the particle tends to evolve from mode I to mode IV with the increase in  $Gr$  at various  $Re$ . However, there are some exceptions. For example, the motion mode of the particle at  $Re = 700$  goes through mode I and mode II successively with an increasing  $Gr$ . However, when  $Gr$  is over  $3 \times 10^5$ , it shows a long transition stage, in which the different particle motion modes could arise alternately. Then the particle keeps in the stable mode IV motion as the  $Gr$  exceeds  $1 \times 10^6$ . Again, this indicates that the particle motion of mode III could be an unstable state when both the buoyancy effect and the lid-driven effect are non-negligible, which has been discussed in Sec. VB3. In addition, the intense buoyancy effect for the high  $Gr$  also complicates the particle motion before it moves along the stable orbit, which enhances the instability of the particle motion mode.

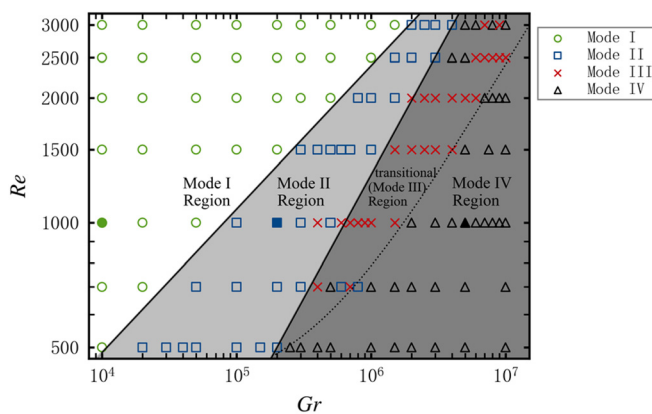


**FIG. 17.** The diagram of motion mode of neutrally buoyant particle released at  $(0.25L, 0.25L)$  in the thermal two-sided lid-driven cavity flow for  $10^4 \leq Gr \leq 10^7$  and  $500 \leq Re \leq 3000$ . The solid marks also denote the results when the particle is released at  $(0.75L, 0.75L)$ .

The motion behavior of the particle can be identified as four regions in the parameter space of  $Gr$  and  $Re$ , i.e., mode I, mode II, mode III (or transitional region), and mode IV regions, as shown in Fig. 17. Critical lines can be observed among the four regions, which can reflect the functional relationship of the critical  $Gr$  to  $Re$  and allow for the prediction of the motion mode of the particle suppose that  $Gr$  and  $Re$  are given. In order to quantify the relationship, the least-square fitting is implemented and a power-law correlation of critical  $Gr$  and  $Re$  can be similarly established according to Liu *et al.*<sup>30</sup>

$$Gr = aRe^b, \tag{30}$$

where  $a$  and  $b$  are the fitting parameters. For the transition of mode I, the parameters take the value of  $a = 1.092 \times 10^{-4}$  and  $b = 2.919$  in the range of  $500 \leq Re \leq 3000$ . Then, for the transition of mode II, the parameters take the value of  $a = 3.728$  and  $b = 1.729$ , which are validated for  $500 \leq Re \leq 3000$ . However, the correlation of critical  $Gr$  and  $Re$  for the mode III is not given, due to the instability of particle motion mode. In addition, it can be observed that the critical  $Gr$  increases with  $Re$  as shown in Fig. 18. Equation (30) quantitatively reflects the competition between  $Gr$  and  $Re$ . The increase in  $Re$  delays the evolution of the mode of particle motion. Furthermore, the motion modes of the particle in the mode III region (transitional region) are obtained based on the initial position of  $(0.25L, 0.25L)$ , aligning with the initial position setting in the other regions. The motions of the particle released from  $(0.75L, 0.75L)$  are also examined for several  $Gr$  and  $Re$  in the other regions as shown in Fig. 17, which shows the similar steady motion mode. Hence, the regime-map in Fig. 17 can be used to identify the steady motion mode of particle for various  $Gr$  and  $Re$ . It should be noted, however, in the transitional region, the motion of the particle strongly depends on the initial position of the particle.

To further understand the physics underlying Eq. (30), we can rewrite the formula as  $Gr/Re^b = a$ . When  $b = 2$ , the left part can be regarded as the Richardson number, characterizing the thermal convection of fluid flow. This has been validated in several other research on the mixed convection in cavity flows,<sup>49,50</sup> in which the competition between buoyancy-driven natural convection and lid-driven forced

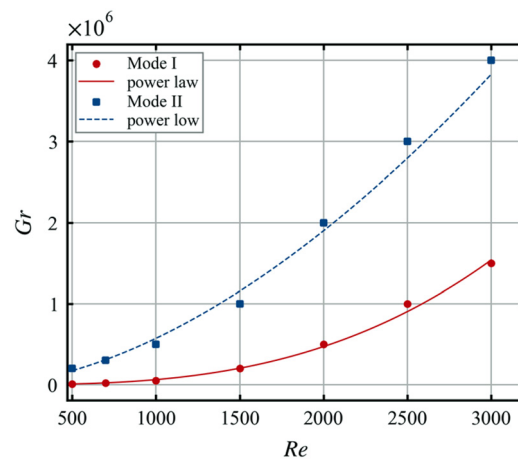


**FIG. 18.** The critical value of  $Gr$  for particle motion mode transitions against  $Re$ .



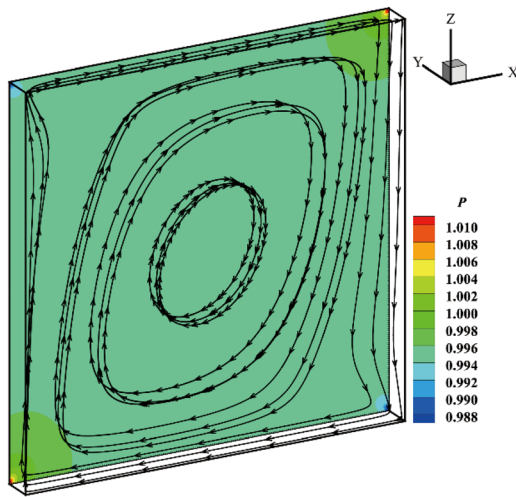


FIG. 19. The flow patterns of the quasi-two-dimensional two-sided lid-driven cavity flow for  $Re = 200$ .

convection dominates the fluid flow, and can be quantified by the ratio of  $Gr$  to  $Re^2$ . However, the exponent  $b$  may not be exactly 2 for the particle-laden systems, because of the finite-size of the particle. It might be attributed to the inertia of the particle, relating to the particle size and density. The mismatch of the particle density to the fluid density could enhance the effects of buoyancy and inertia.<sup>19</sup> In addition, the particle size also significantly influences the particle motion in fluid flow. It is shown that some crucial factors, e.g., the Stokes number<sup>18,19</sup> and lift force<sup>30,31,51</sup> exerted on the particle in the shear flow, could depend strongly on the particle size. Hence, the effects of particle size and particle density deserve further investigation in the near future.

### E. The three-dimensional cavity flow with a spherical particle

In this section, the motion behavior of a spherical particle in a quasi-two-dimensional two-sided lid-driven cavity flow with thermal convection is studied, to qualitatively verify the practical significance of the two-dimensional studies in revealing the particle motion in the confined fluid flow with thermal convection. The setup and numerical method are shown in Appendix A, and the grid independence validation is conducted in Appendix B. The pure cavity flow is obtained beforehand, and the flow pattern for  $Re = 200$  is shown in Fig. 19. The platelike streamlines can be observed in  $y$ -direction, while the symmetrical vortex structures are formed in the  $xz$ -plane. The quasi-two-dimensional fluid flow is expected to induce the similar particle motion compared with the pure two-dimensional fluid flow.

Then, the motion of a sphere in the cavity flow is further studied. Figure 20(a) shows the simulation results with  $Re = 200$  and  $Gr = 400$ . As can be seen, the particle motion in  $y$ -direction is negligible, while the trajectories in the  $xz$ -plane show the periodicity at steady state. Hence, the particle exhibits a quasi-two-dimensional motion in the  $xz$ -plane. In addition, Fig. 20(b) shows the flow patterns and temperature distribution at the middle cross section along  $y$ -direction. As shown, the low temperature zone can be found around the particle and the bulk of the cavity flow maintains high temperature  $T_h$ . The streamlines are quite similar to the pure cavity flow as shown in Fig. 19. This suggest that the nature convection poses negligible effect on the heat transfer and fluid flow at low  $Gr$ .

Furthermore, it can be observed that the particle could have different motion behavior for different  $Re$  and  $Gr$ . Figure 21(a) depicts the steady trajectories of the particle at various  $Re$  and  $Gr$ . For  $Re = 100$ , the increase in  $Gr$  will lead to that the symmetrical limit cycle like orbit at lower  $Gr$  gradually deforms in the top-left corner and then migrates to the bottom-left corner of the cavity, which exhibits the motion behavior from mode I to mode II and then to mode IV.

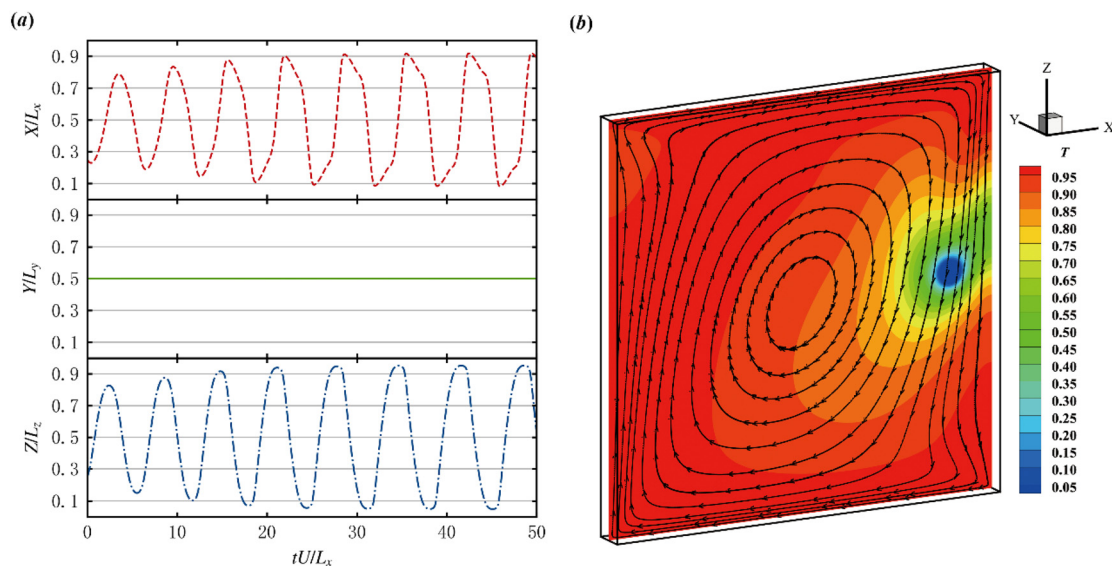
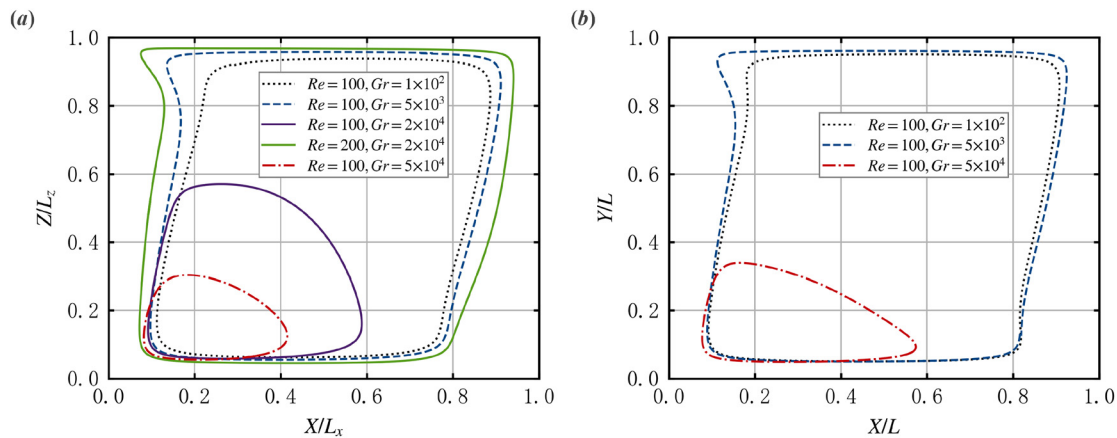


FIG. 20. The motion of a spherical particle in the quasi-two-dimensional two-sided lid-driven cavity flow at  $Re = 200$  and  $Gr = 400$ : (a) the trajectory of the particle in  $x$ -,  $y$ -, and  $z$ -direction and (b) the snapshot of the fluid flow and temperature contours at  $tU/L_x = 50$ .



**FIG. 21.** The steady trajectory of the particle in the two-sided lid-driven cavity flow with thermal convection at various  $Re$  and  $Gr$ : (a) quasi-two-dimensional configuration and (b) two-dimensional configuration.

This indicates that the enhanced natural convection with the increase in  $Gr$  can affect the trajectory of the particle in the form of the limit cycle orbit. In addition, the particle shows a mode IV like orbit for  $Gr = 2 \times 10^4$  at  $Re = 100$  while a mode II like trajectory at  $Re = 200$ . This means that the higher  $Re$  would delay the evolution of particle motion as the results of the competition between natural convection and forced convection. Figure 21(b) shows steady trajectories of the particle for  $Re = 100$  in the pure two-dimensional configuration, and the similar motion mode can be observed at the corresponding  $Gr$  despite some minor yet detailed differences ascribed to the different surface area to volume ratio in the two configurations. Figure 22 shows the snapshots of flow pattern and temperature distribution at the middle cross section for  $Gr = 5 \times 10^3$  and  $5 \times 10^4$  at  $Re = 100$ . At  $Gr = 5 \times 10^3$ , the regular vortex structure of the cavity flow with the low-temperature zone following the particle can be observed, while at  $Gr = 5 \times 10^4$  the stratification of the cavity flow in which the particle moves in the bottom layer can be identified. These are essentially the

characteristics of flow pattern and temperature distribution in mode II and mode IV, according to the discussions in Secs. VB 2 and VB 4.

The two-dimensional study in the present work establishes the diagram and regime-map as shown in Fig. 17 that can distinguish the particle motion with four modes in the parameter space of  $Gr$  and  $Re$ . Our quasi-two-dimensional simulation results show that the motion of the spherical particle as well as the temperature field for the three-dimensional (quasi-two-dimensional) two-sided lid-driven cavity flow displays some similar characteristics with that for the two-dimensional cases. Indeed, some minor yet detailed differences of the trajectories or the heat and fluid flow may be found because of the different surface area to volume ratio as well as different momentum and heat transfer. However, the same mode of the particle motion can be observed for corresponding parameters, and this is due to that underlying physics keeps the same, i.e., the competition of the forced and natural convection. Hence, the two-dimensional results can be used to illustrate the thermal effects dominated by either natural or forced convection and

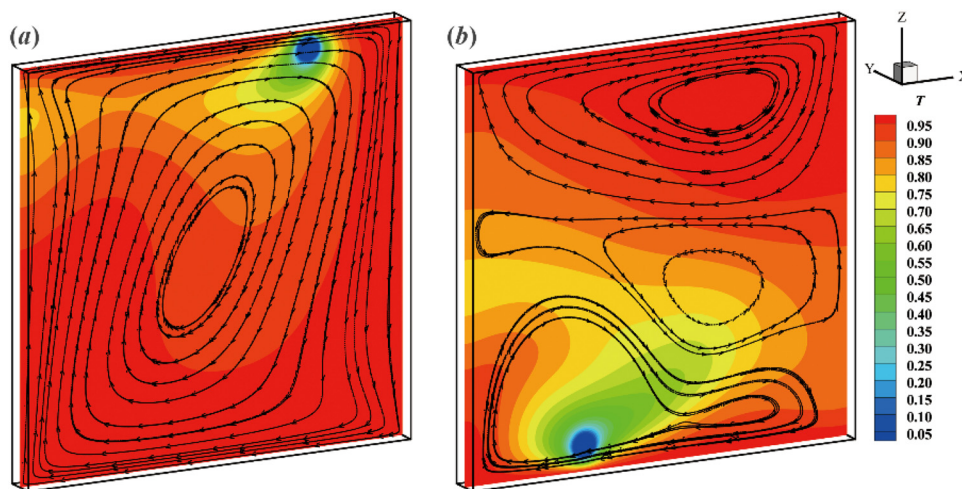


**FIG. 22.** The snapshots of the flow pattern and temperature distribution at the middle cross section for  $Re = 100$ : (a)  $Gr = 5 \times 10^3$  and  $tU/L_x = 100$ ; and (b)  $Gr = 5 \times 10^4$  and  $tU/L_x = 50$ .

have the practical indication for three-dimensional particle motion in the confined fluid flow with thermal convection. As the full three-dimensional simulations with higher  $Re$  would significantly increase computational cost, here we only consider the quasi-two-dimensional cases with lower  $Re$  to guarantee reasonable computational efficiency. Nevertheless, the preliminary comparison between two-dimensional and quasi-two-dimensional simulation results at a relatively low  $Re = 100$  added the confidence in analogy of the two-dimensional two-sided lid-driven cavity thermal flows and particle motions to the three-dimensional in this work. A systematic three-dimensional simulation study with higher  $Re$  and  $Gr$ , however, will remain as a further task in the near future to quantitatively verify our findings in current two-dimensional simulations.

VI. CONCLUSION

A thermal lattice Boltzmann model coupled with the immersed boundary method has been used to study the motion of a circular neutrally buoyant cold particle in the two-sided lid-driven thermal cavity flow. The code is validated by examining the particle settling in a channel with thermal convection. The effects of cavity Grashof number  $Gr$  and Reynolds number  $Re$  on the dynamics of the particle are studied. It shows that the particle motion in the cavity flow demonstrates four particle motion modes at  $Re = 500-3000$  and  $Gr = 10^4-10^7$ : in mode I, the particle manifests the periodic steady motion in the periphery of cavity, in mode II, it moves along a orbit deformed in the top-left corner of cavity, in mode III, the particle migrates to the corner eddy in the top-left corner of the cavity, and in mode IV, the particle migrates to the bottom-left part of the cavity and might shrink into a fix point. A diagram for the four motion modes of single particle is obtained. The physics behind the transition of motion modes lies in the competition between the natural convection and the forced convection, which, eventually, are, respectively, dominated by the buoyancy effect and fluid inertia. In addition, it is shown that the particle motion modes can be altered in the mode III region, which could be related to the initial position, showing that the particle motion of mode III could be an unstable state. The critical  $Gr$  is identified to present the transition between different modes and is further formulated by a power law correlation with regard to the cavity  $Re$ . Finally, the simulations of three-dimensional configuration are implemented, which qualitatively verify the practical significance of the two-dimensional studies in revealing the particle motion in the confined fluid flow with thermal convection. In view of only two-dimensional simulations being conducted in this work, it is expected that three-dimensional simulations with higher  $Re$  and  $Gr$  for particle motion in two-sided lid-driven cavity thermal flow will be a further task in the near future to quantitatively verify our findings in current two-dimensional simulations.

ACKNOWLEDGMENTS

The authors would like to thank the National Natural Science Foundation of China (Nos. 22293021, 21991093, and 22288101) for supporting this work.

AUTHOR DECLARATIONS

Conflict of Interest

The authors have no conflicts to disclose.

Author Contributions

**Yunxin Zhang:** Conceptualization (equal); Data curation (equal); Formal analysis (equal); Investigation (equal); Software (equal); Validation (equal); Writing – original draft (equal). **Chenggong Li:** Investigation (equal); Software (equal); Supervision (equal); Writing – review & editing (equal). **Mao Ye:** Funding acquisition (equal); Project administration (equal); Resources (equal); Supervision (equal); Writing – review & editing (equal).

DATA AVAILABILITY

The data that support the findings of this study are available from the corresponding author upon reasonable request.

APPENDIX: A. THE SETUP AND NUMERICAL METHOD FOR THE THREE-DIMENSIONAL CAVITY

A quasi-two-dimensional two-sided lid-driven cavity flow containing a freely moving sphere is considered, as shown in Fig. 23(a), to illustrate the similarity between then pure two-dimensional and quasi-two-dimensional simulations. The length of the cavity in  $x$ - and  $z$ -direction is set as 20 times the particle diameter, and the thickness of the cavity is 1.6 times the particle diameter. The incompressible Newtonian fluid in the cavity is driven by the top and bottom walls moving along the opposite direction with the velocity of  $U$  and  $-U$ , respectively. The non-slip boundary condition is set for the two side walls at  $x = 0$  and  $x = L_x$  (i.e.,  $\mathbf{u} = 0$ ), while free-slip boundaries are set for the side walls at  $y = 0$  and  $y = L_y$  (i.e.,  $\partial u_x / \partial y = \partial u_z / \partial y = u_y = 0$ ). The top and bottom walls maintain a temperature of  $T_h$ , and the other four side walls are adiabatic. The temperature of the sphere is set as  $T_c$ .

To study the particle motion in the cavity flow with thermal convection, the sphere is released in the cavity at location  $(0.25L_x, 0.5L_y, 0.25L_z)$  after the fluid flow reaches a steady state. The Navier–Stokes equation as shown in Eqs. (1)–(3) has been considered as the governing equation of the fluid flow. In order to solve the quasi-two-dimensional fluid flow, the thermal lattice Boltzmann method with D3Q15 model<sup>34,52</sup> is adopted. The evolution equations for particle distribution function and thermal energy distribution function are written as Eqs. (9) and (10), respectively. The discrete velocity  $\mathbf{e}_i$  in the three-dimensional model is

$$\mathbf{e}_i = \begin{cases} (0, 0), & i = 0, \\ (\pm 1, 0, 0), (0, \pm 1, 0), (0, 0, \pm 1), & i = 1 \text{ to } 6, \\ (\pm 1, \pm 1, \pm 1), & i = 7 \text{ to } 14. \end{cases} \quad (A1)$$

In addition, the corresponding equilibrium distribution functions  $f_i^{eq}(\mathbf{r}, t)$  and  $g_i^{eq}(\mathbf{r}, t)$  are, respectively, defined by

$$f_i^{eq} = \omega_i \rho_f \left[ 1 + \frac{3\mathbf{e}_i \cdot \mathbf{u}}{c^2} + \frac{9(\mathbf{e}_i \cdot \mathbf{u})^2}{2c^4} - \frac{3\mathbf{u}^2}{2c^2} \right] \quad (A2)$$

and

$$g_i^{eq} = \begin{cases} -\frac{\rho_f T \mathbf{u}^2}{3c^2}, & i = 0, \\ \frac{\rho_f T}{9} \left[ 1 + \frac{\mathbf{e}_i \cdot \mathbf{u}}{c^2} + \frac{9(\mathbf{e}_i \cdot \mathbf{u})^2}{2c^4} - \frac{3\mathbf{u}^2}{2c^2} \right], & i = 1 \text{ to } 6, \\ \frac{\rho_f T}{72} \left[ 3 + 7\frac{\mathbf{e}_i \cdot \mathbf{u}}{c^2} + \frac{9(\mathbf{e}_i \cdot \mathbf{u})^2}{2c^4} - \frac{3\mathbf{u}^2}{2c^2} \right], & i = 7 \text{ to } 14, \end{cases} \quad (A3)$$

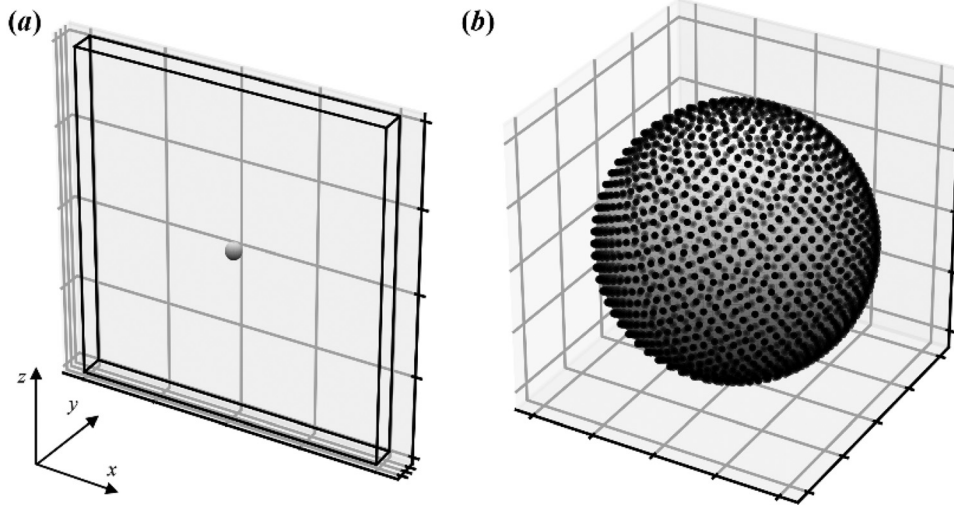


**FIG. 23.** The sketch of a sphere moving in the quasi-two-dimensional two-sided lid-driven cavity flow: (a) the computational domain and (b) the distribution of Lagrangian points on the surface of the sphere.

where the weight coefficients  $\omega_i$  are set as  $\omega_0 = 2/9$ ,  $\omega_{1-6} = 1/9$ , and  $\omega_{7-14} = 1/72$ . The macroscopic variables can be obtained by

$$\rho_f = \sum_i f_i, \tag{A4}$$

$$\rho_f \mathbf{u} = \sum_i \mathbf{e}_i f_i + \frac{\delta_t}{2} \mathbf{F}, \tag{A5}$$

$$\rho_f T = \sum_i g_i + \frac{\delta_t}{2} Q. \tag{A6}$$

The sphere is treated by a set of Lagrangian points follows the Fibonacci lattice,<sup>52</sup> as shown in Fig. 23(b), which can be numerically described as

$$\psi = \frac{2l}{2N+1}, \quad l \in [-N, N], \tag{A7}$$

$$\begin{cases} x_l = r\sqrt{1-\psi^2}\cos(2\pi l\xi) + c_x, \\ y_l = r\sqrt{1-\psi^2}\sin(2\pi l\xi) + c_y, \\ z_l = r\psi + c_z, \end{cases} \tag{A8}$$

where  $2N+1$  is the number of the Lagrangian points with coordinates  $(x_l, y_l, z_l)$ ,  $(c_x, c_y, c_z)$  represents the coordinate of sphere center, and  $\xi = (\sqrt{5}-1)/2$ . The interaction between particle and fluid flow is treated by the immersed boundary method according to Eqs. (21)–(27). Note that the discrete delta function is written by  $D(\mathbf{r} - \mathbf{X}_b) = \delta(x - x_b)\delta(y - y_b)\delta(z - z_b)$ , and the following equations are used to solve both the translational and rotational motion of the sphere:<sup>53</sup>

$$\frac{d}{dt} \begin{bmatrix} \mathbf{X}_p(t) \\ \mathbf{q}(t) \\ \mathbf{P}(t) \\ \mathbf{L}(t) \end{bmatrix} = \begin{bmatrix} \mathbf{V}_p(t) \\ \frac{1}{2}\omega_p \mathbf{q}(t) \\ \mathbf{F}_p(t) \\ \mathbf{T}_p(t) \end{bmatrix}, \tag{A9}$$

where  $\mathbf{q}(t)$  is the unit quaternion form for the rotational motion matrix,  $\mathbf{P}(t)$  is the linear momentum, and  $\mathbf{L}(t)$  is the angular momentum of the sphere. Thus, both the translational and

rotational velocity of the spherical particle can be calculated via  $\mathbf{V}_p = \mathbf{P}/M$  and  $\omega_p = \mathbf{I}^{-1}\mathbf{L}$ , where  $M$  is the mass of the spherical particle,  $\mathbf{I}$  is the inertia matrix of the sphere as shown in the following:

$$\mathbf{I} = \begin{bmatrix} \frac{2}{5}MR^2 & 0 & 0 \\ 0 & \frac{2}{5}MR^2 & 0 \\ 0 & 0 & \frac{2}{5}MR^2 \end{bmatrix}. \tag{A10}$$

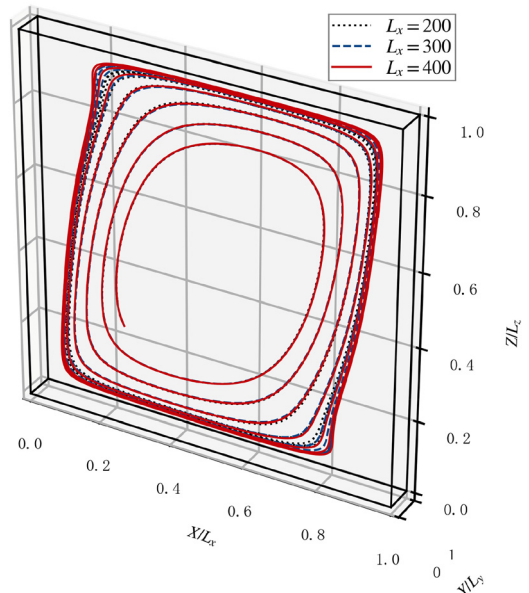


**FIG. 24.** The trajectories of a sphere moving in the two-sided lid-driven cavity flow for various grid sizes at  $Re = 200$  and  $Gr = 400$ .



## APPENDIX B: THE GRID INDEPENDENCE VALIDATION FOR THE THREE-DIMENSIONAL CONFIGURATION

Due to the limitations of computational efficiency and convergence, we have implemented the simulations with small grid size and low  $Re$ . The grid dependence validation has been conducted with the grid size of  $L_x = 200, 300,$  and  $400$  with  $Re = 200$  and  $Gr = 400$ , respectively. The trajectories of the sphere for various grid sizes are shown in Fig. 24. These trajectories are in general consistent, with some minor difference at the top-left and bottom-right corners. This can be ascribed to the complex fluid flows at these corners that require finer grid to in the simulations. In the subsequent simulations, however, the grid size of  $L_x = 200$  is chosen for the balance of computational cost and simulation resolution. We would argue that the quasi-two-dimensional motion of the particle in two-sided lid-driven cavity flow with thermal condition could be reflected at coarse grid.

## REFERENCES

- <sup>1</sup>N. G. Deen, S. H. L. Kriebitzsch, M. A. van der Hoef, and J. A. M. Kuipers, "Direct numerical simulation of flow and heat transfer in dense fluid-particle systems," *Chem. Eng. Sci.* **81**, 329 (2012).
- <sup>2</sup>Z.-G. Feng and S. G. Musong, "Direct numerical simulation of heat and mass transfer of spheres in a fluidized bed," *Powder Technol.* **262**, 62 (2014).
- <sup>3</sup>G. Yue, R. Cai, J. Lu, and H. Zhang, "From a CFB reactor to a CFB boiler—The review of R&D progress of CFB coal combustion technology in China," *Powder Technol.* **316**, 18–28 (2017).
- <sup>4</sup>P. N. Shankar and M. D. Deshpande, "Fluid mechanics in the driven cavity," *Annu. Rev. Fluid Mech.* **32**, 93 (2000).
- <sup>5</sup>J. Mellmann, "The transverse motion of solids in rotating cylinders-forms of motion and transition behavior," *Powder Technol.* **118**, 251 (2001).
- <sup>6</sup>J. J. Derksen, "Solid particle mobility in agitated Bingham liquids," *Ind. Eng. Chem. Res.* **48**, 2266 (2009).
- <sup>7</sup>D. A. Zumbrennen, K. C. Miles, and Y. H. Liu, "Auto-processing of very fine-scale composite materials by chaotic mixing of melts," *Composites, Part A* **27**, 37 (1996).
- <sup>8</sup>F. Shen, S. Xue, M. Xu, Y. Pang, and Z. M. Liu, "Experimental study of single-particle trapping mechanisms into microcavities using microfluidics," *Phys. Fluids* **31**, 042002 (2019).
- <sup>9</sup>V. Prasad, A. Sharma, and S. S. Kulkarni, "Lid-driven cavity flow-induced dynamics of a neutrally buoyant solid: Effect of Reynolds number, flexibility, and size," *Phys. Fluids* **34**, 073310 (2022).
- <sup>10</sup>J. Zhang, G. Sun, J. Hu, J. Wu, and M. Xu, "A neutrally buoyant particle captured by vortex in a lid-driven cavity with an internal obstacle," *Phys. Fluids* **34**, 073309 (2022).
- <sup>11</sup>W. R. Hwang, P. D. Anderson, and M. A. Hulsen, "Chaotic advection in a cavity flow with rigid particles," *Phys. Fluids* **17**, 043602 (2005).
- <sup>12</sup>S. J. Tsorngr, H. Capart, J. S. Lai, and D. L. Young, "Three-dimensional tracking of the long time trajectories of suspended particles in a lid-driven cavity flow," *Exp. Fluids* **40**, 314 (2006).
- <sup>13</sup>S. J. Tsorngr, H. Capart, D. C. Lo, J. S. Lai, and D. L. Young, "Behaviour of macroscopic rigid spheres in lid-driven cavity flow," *Int. J. Multiphase Flow* **34**, 76 (2008).
- <sup>14</sup>F. Shen, M. Ai, Z. Li, S. Xue, M. Xu, and Z. Liu, "Particle orbiting motion and deviations from streamlines in a microvortex," *Appl. Phys. Lett.* **120**, 024101 (2022).
- <sup>15</sup>P. Kosinski, A. Kosinska, and A. C. Hoffmann, "Simulation of solid particles behaviour in a driven cavity flow," *Powder Technol.* **191**, 327 (2009).
- <sup>16</sup>F. Romanò and H. C. Kuhlmann, "Particle-boundary interaction in a shear-driven cavity flow," *Theor. Comput. Fluid Dyn.* **31**, 427 (2017).
- <sup>17</sup>H. C. Kuhlmann, M. Wanschura, and H. J. Rath, "Flow in two-sided lid-driven cavities: Non-uniqueness, instabilities, and cellular structures," *J. Fluid Mech.* **336**, 267 (1997).
- <sup>18</sup>F. Romanò, P. Kunchi Kannan, and H. C. Kuhlmann, "Finite-size Lagrangian coherent structures in a two-sided lid-driven cavity," *Phys. Rev. Fluid* **4**, 024302 (2019).
- <sup>19</sup>H. Wu, F. Romanò, and H. C. Kuhlmann, "Attractors for the motion of a finite-size particle in a two-sided lid-driven cavity," *J. Fluid Mech.* **906**, 906 (2021).
- <sup>20</sup>H. Wu, F. Romanò, and H. C. Kuhlmann, "Attractors for the motion of a finite-size particle in a cuboidal lid-driven cavity," *J. Fluid Mech.* **955**, A16 (2023).
- <sup>21</sup>J. Hu, "Motion of a neutrally buoyant circular particle in a clockwise double-lid-driven square cavity," *Phys. Fluids* **32**, 113304 (2020).
- <sup>22</sup>T. Rosemann, B. Kravets, S. R. Reinecke, H. Kruggel-Emden, M. Wu, and B. Peters, "Comparison of numerical schemes for 3D lattice Boltzmann simulations of moving rigid particles in thermal fluid flows," *Powder Technol.* **356**, 528 (2019).
- <sup>23</sup>R. Safa, A. Soltani Goharrizi, S. Jafari, and E. Jahanshahi Javaran, "On the evaluation of heat and mass transfer effects on the migration behavior of neutrally buoyant particles in a Couette flow," *Int. J. Heat Mass Transfer* **144**, 118659 (2019).
- <sup>24</sup>J. W. S. McCullough, S. M. Aminossadati, and C. R. Leonardi, "Transport of particles suspended within a temperature-dependent viscosity fluid using coupled LBM-DEM," *Int. J. Heat Mass Transfer* **149**, 119159 (2020).
- <sup>25</sup>Z.-G. Feng and E. E. Michaelides, "Inclusion of heat transfer computations for particle laden flows," *Phys. Fluids* **20**, 040604 (2008).
- <sup>26</sup>H. U. I. Gan, J. Chang, J. J. Feng, and H. H. Hu, "Direct numerical simulation of the sedimentation of solid particles with thermal convection," *J. Fluid Mech.* **481**, 385 (2003).
- <sup>27</sup>B. Yang, S. Chen, C. Cao, Z. Liu, and C. Zheng, "Lattice Boltzmann simulation of two cold particles settling in Newtonian fluid with thermal convection," *Int. J. Heat Mass Transfer* **93**, 477 (2016).
- <sup>28</sup>J. Hu and Z. Guo, "A numerical study on the migration of a neutrally buoyant particle in a Poiseuille flow with thermal convection," *Int. J. Heat Mass Transfer* **108**, 2158 (2017).
- <sup>29</sup>G. Segré and A. Silberberg, "Radial particle displacements in Poiseuille flow of suspensions," *Nature* **189**, 209 (1961).
- <sup>30</sup>W. Liu and C.-Y. Wu, "Inertial migration of a neutrally buoyant circular particle in a planar Poiseuille flow with thermal fluids," *Phys. Fluids* **33**, 063315 (2021).
- <sup>31</sup>W. Liu and C.-Y. Wu, "Lateral migration of a neutrally buoyant particle in Couette flow with thermal convection," *Int. J. Multiphase Flow* **138**, 103612 (2021).
- <sup>32</sup>D. Kashyap, A. K. Dass, H. F. Oztop, and N. Abu-Hamdeh, "Multiple-relaxation-time lattice Boltzmann analysis of entropy generation in a hot-block-inserted square cavity for different Prandtl numbers," *Int. J. Therm. Sci.* **165**, 106948 (2021).
- <sup>33</sup>S. K. Kang and Y. A. Hassan, "A direct-forcing immersed boundary method for the thermal lattice Boltzmann method," *Comput. Fluids* **49**, 36 (2011).
- <sup>34</sup>Z. Chen, C. Shu, L. M. Yang, X. Zhao, and N. Y. Liu, "Immersed boundary-simplified thermal lattice Boltzmann method for incompressible thermal flows," *Phys. Fluids* **32**, 013605 (2020).
- <sup>35</sup>Y. Peng, C. Shu, and Y. T. Chew, "Simplified thermal lattice Boltzmann model for incompressible thermal flows," *Phys. Rev. E* **68**, 026701 (2003).
- <sup>36</sup>Z. Guo, B. Shi, and N. Wang, "Lattice BGK model for incompressible Navier-Stokes equation," *J. Comput. Phys.* **165**, 288 (2000).
- <sup>37</sup>X. He, S. Chen, and G. D. Doolen, "A novel thermal model for the lattice Boltzmann method in incompressible limit," *J. Comput. Phys.* **146**, 282 (1998).
- <sup>38</sup>J. Wang, M. Wang, and Z. Li, "A lattice Boltzmann algorithm for fluid-solid conjugate heat transfer," *Int. J. Therm. Sci.* **46**, 228 (2007).
- <sup>39</sup>Z. Guo, C. Zheng, and B. Shi, "Non-equilibrium extrapolation method for velocity and pressure boundary conditions in the lattice Boltzmann method," *Chin. Phys. Lett.* **11**, 366 (2002).
- <sup>40</sup>C. S. Peskin, "Flow patterns around heart valves: A numerical method," *J. Comput. Phys.* **10**, 252 (1972).
- <sup>41</sup>C. S. Peskin, "Numerical analysis of blood flow in the heart," *J. Comput. Phys.* **25**, 220 (1977).
- <sup>42</sup>R. Mittal and G. Iaccarino, "Immersed boundary methods," *Annu. Rev. Fluid Mech.* **37**, 239 (2005).
- <sup>43</sup>Z. Guo, C. Zheng, and B. Shi, "Discrete lattice effects on the forcing term in the lattice Boltzmann method," *Phys. Rev. E* **65**, 046308 (2002).



- <sup>44</sup>R. Glowinski, T. W. Pan, T. I. Hesla, D. D. Joseph, and J. Périaux, "A fictitious domain approach to the direct numerical simulation of incompressible viscous flow past moving rigid bodies: Application to particulate flow," *J. Comput. Phys.* **169**, 363 (2001).
- <sup>45</sup>Z.-G. Feng and E. E. Michaelides, "The immersed boundary-lattice Boltzmann method for solving fluid-particles interaction problems," *J. Comput. Phys.* **195**, 602 (2004).
- <sup>46</sup>Z. Yu, X. Shao, and A. Wachs, "A fictitious domain method for particulate flows with heat transfer," *J. Comput. Phys.* **217**, 424 (2006).
- <sup>47</sup>A. Eshghinejadfard and D. Thévenin, "Numerical simulation of heat transfer in particulate flows using a thermal immersed boundary lattice Boltzmann method," *Int. J. Heat Fluid Flow* **60**, 31 (2016).
- <sup>48</sup>D. A. Perumal and A. K. Dass, "Simulation of flow in two-sided lid-driven square cavities by the lattice Boltzmann method," *7th International Conference on Advances in Fluid Mechanics* (WIT Press, 2008), Vol. 59, p. 45.
- <sup>49</sup>R. Iwatsu, J. M. Hyun, and K. Kuwahara, "Mixed convection in a driven cavity with a stable vertical temperature gradient," *Int. J. Heat Mass Transfer* **36**, 1601 (1993).
- <sup>50</sup>O. Aydin, "Aiding and opposing mechanisms of mixed convection in a shear- and buoyancy-driven cavity," *Int. Commun. Heat Mass Transfer* **26**, 1019 (1999).
- <sup>51</sup>D. Di Carlo, J. F. Edd, K. J. Humphry, H. A. Stone, and M. Toner, "Particle segregation and dynamics in confined flows," *Phys. Rev. Lett.* **102**, 094503 (2009).
- <sup>52</sup>Y. Peng, C. Shu, and Y. T. Chew, "A 3D incompressible thermal lattice Boltzmann model and its application to simulate natural convection in a cubic cavity," *J. Comput. Phys.* **193**, 260 (2004).
- <sup>53</sup>Z.-G. Feng and E. E. Michaelides, "Proteus: A direct forcing method in the simulations of particulate flows," *J. Comput. Phys.* **202**, 20 (2005).